JOURNAL OF GEOPHYSICAL RESEARCH, VOL. 111, C06038, doi:10.1029/2005JC003324, 2006

Click Here for Full Article

An assessment of buoy-derived and numerical weather prediction surface heat fluxes in the tropical Pacific

Meghan F. Cronin,[1] Christopher W. Fairall,[2] and Michael J. McPhaden[1]

Received 7 October 2005; revised 24 January 2006; accepted 17 March 2006; published 28 June 2006.

[1] As part of the Eastern Pacific Investigation of Climate Processes program, from 2000 through 2003, the easternmost 95°W Tropical Atmosphere Ocean (TAO) moorings were enhanced to provide time series of net surface heat flux, and the National Oceanic and Atmospheric Administration ship maintaining the 95°W and 110°W TAO lines was enhanced to monitor surface heat fluxes and atmospheric boundary layer structure. In this study we compare the ship-based and buoy-based radiative, bulk latent, and sensible heat fluxes, as well as the meteorological state variables used to compute the turbulent heat fluxes. The buoy net surface heat flux measurements appear to have an overall uncertainty near the target 10 W m^{-2}, when careful attention is paid to the state variables. When hourly averaged data were unavailable, the telemetered daily averaged data were used in combination with an estimate of the mesoscale gustiness. In the eastern tropical Pacific a warm layer correction to account for stratification above 1-m depth was important only during the warm season (January–May) near the equator. These high-quality, cross-validated buoy heat flux time series are then used to assess the National Centers for Environmental Prediction/National Center for Atmospheric Research (NCEP/NCAR), NCEP/Department of Energy, and 40-year European Centre for Medium-Range Weather Forecasts reanalyses' surface heat fluxes. All reanalyses show that over warm water where deep convection is prominent, latent heat loss is too large and net solar radiation is too weak; conversely, in regions of stratocumulus over cool water, net solar radiation is too strong, and for NCEP/NCAR, latent heat loss is too weak.

Citation: Cronin, M. F., C. W. Fairall, and M. J. McPhaden (2006), An assessment of buoy-derived and numerical weather prediction surface heat fluxes in the tropical Pacific, *J. Geophys. Res.*, *111*, C06038, doi:10.1029/2005JC003324.

1. Introduction

[2] The oceans play an important role in climate by storing, transporting, and releasing heat to the atmosphere. In situ measurements of the air-sea heat flux derive primarily from ship-based measurements or from buoy measurements. While research ships can carry a full suite of sensors to monitor the surface fluxes and atmospheric boundary layer structure, as well as a cadre of scientists to tend these sensors, the measurements are often too sparse to use to assess regional and global flux products. In contrast, surface meteorological and oceanic data from the Tropical Atmosphere Ocean/Triangle Trans-Ocean buoy Network (TAO/TRITON) buoy array in the tropical Pacific [*McPhaden et al.*, 1998] and the Pilot Research moored Array in the Tropical Atlantic (PIRATA) buoy array in the tropical Atlantic [*Servain et al.*, 1998] are widely used for assessing satellite, general circulation model, and numerical weather prediction (NWP) fields [*Vialard et al.*, 2003; *Gentemann et al.*, 2004; *Jiang et al.*, 2005]. Surface heat fluxes computed from the moorings support a wide range of oceanographic and meteorological studies [*Cronin and McPhaden*, 1997; *Sui et al.*, 2003; *DeSzoeke et al.*, 2005]. In this study we attempt to cross-validate ship-based and mooring meteorological variables and air-sea flux components. The cross-validation and careful attention to methodology by which the fluxes are computed then allow these data to be used with confidence as a benchmark data set for validation studies. Recently, during the Eastern Pacific Investigation of Climate Processes (EPIC) the easternmost TAO line was enhanced with additional sites and a suite of sensors to provide a picket-fence time series of the air-sea heat, moisture, and momentum fluxes, as well as the upper ocean temperature, salinity, and horizontal currents. In addition, during the EPIC program, the National Oceanic and Atmospheric Administration (NOAA) ship that tended the TAO 95°W and 110°W moorings at 6-month intervals was equipped with sensors to monitor fluxes and boundary layer conditions [*Hare et al.*, 2005]. While two full sea days are devoted to ship-buoy intercomparisons at Woods Hole IMET moorings (one day prior to mooring recovery and one day following

[1] Pacific Marine Environmental Laboratory, NOAA, Seattle, Washington, USA.
[2] Earth System Research Laboratory, NOAA, Boulder, Colorado, USA.

This paper is not subject to U.S. copyright.
Published in 2006 by the American Geophysical Union.

mooring deployment), a similar procedure was not feasible on the TAO tender cruises since typically 7–10 mooring recovery and deployment operations are performed on each cruise. The comparison is thus not a controlled experiment and the results depend not only upon the accuracy of the sensors, but also upon different space/time sampling characteristics of the ship and buoy measurement systems.

[3] The eastern tropical Pacific near the Pan-American landmass is characterized by southerly winds that extend from the cool waters in the stratus deck region off South America, across the equatorial cold tongue, to the convective region of the intertropical convergence zone (ITCZ) where surface waters are warmer than 27°C. Thus although our analysis is focused upon the far eastern Pacific data set, a broad range of conditions are observed, providing a challenging test for intercomparison studies. In addition, a number of issues are raised and addressed regarding the calculation of turbulent fluxes from the TAO buoy measurements, including treatment of gaps in data, the use of daily averaged data in regions with substantial mesoscale gustiness, and the treatment of the bulk sea surface variables in regions of strong currents and/or near-surface stratification.

[4] These cross-validated buoy data can then be used as a benchmark in validation studies. Following the studies of *Jiang et al.* [2005] and *Cronin et al.* [2006], we focus on the surface heat flux fields provided by the Numerical Weather Prediction (NWP) reanalyses, specifically the National Centers for Environmental Prediction/National Center for Atmospheric Research (NCEP/NCAR) Reanalysis [*Kalnay et al.*, 1996], the NCEP/Department of Energy (NCEP/DOE) Reanalysis [*Kanamitsu et al.*, 2002], and the European Centre for Medium-Range Weather Forecasts (ECMWF) 40-year Reanalysis. These reanalyses are all widely used. Understanding both the spatial and seasonal distribution of their biases is important for the climate analyses resulting from these products and is a requisite for model improvement.

2. Background

[5] Net heat exchange between the atmosphere and ocean, Q_0, comprises the net shortwave and longwave radiative fluxes (*Qsw* and *Qlw*), latent heat of evaporation (*Qlat*), and sensible heat fluxes due to different temperatures of air and water (*Qsen*) and of rain and water (*Qrain*):

$$Q_0 = Qsw - Qlw - Qlat - Qsen - Qrain. \quad (1)$$

Net solar radiation *Qsw* is computed by reducing the observed downwelling solar radiation (*SWR*) by the albedo (*a*), that is,

$$Qsw = (1 - a)SWR. \quad (2)$$

Following *Cronin et al.* [1997] we use a constant albedo value of 0.055 [*Fairall et al.*, 1996a]. Net longwave radiation is computed as the difference between the outgoing black-body radiation at the skin temperature, T_s, in degrees Kelvin and the downwelling longwave radiation, reduced by the emissivity (taken here to be a constant $\varepsilon = 0.97$):

$$Qlw = \varepsilon\left(\sigma T_s^4 - LWR\right), \quad (3)$$

where σ is the Stefan Boltzman constant. As will be discussed later, some success has been found in parameterizing the longwave radiation [*Fung et al.*, 1984], in which case an estimate of cloud fraction (from solar radiation), SST, and air temperature and moisture are required. Turbulent heat flux estimates typically require a bulk algorithm and for this we use the *Fairall et al.* [2003] COARE v3.0 algorithm.

[6] The *Fairall et al.* [2003] COARE v3.0 algorithm is based on more than 5000 direct covariance fluxes collected over the global oceans. The algorithm is an outgrowth of the v2.5 bulk algorithm developed for Coupled Ocean Atmosphere and Response Experiment (COARE) [*Fairall et al.*, 1996b], that in turn was based on the *Liu et al.* [1979] parameterizations. The COARE v3.0 algorithm includes updates to the Charnock parameter and roughness length parameterization to increase the range of allowable winds to 0–20 m s^{-1} (rather than 0–10 m s^{-1}). The stable profile functions were updated to give more realistic values in near-stable boundary layer regions such as over the eastern Pacific cold tongue.

[7] As with other Monin-Obukhov similarity theory algorithms, the COARE latent and sensible heat fluxes (and wind stress) are determined by the air minus sea differences in temperature ($T_a - T_s$), mixing ratio (or specific humidity) ($q_a - q_s$), and velocity ($|\boldsymbol{u} - \boldsymbol{u_s}|$). Heights of the air temperature, moisture, and wind sensors can be specified so that, in theory, the log layer profile can be determined either by sensors on a buoy (typically at 2–4 m), on a ship (at 5–15 m), or on an aircraft (at 30–100 m).

[8] Recognizing that the bulk (typically 1-m or 5-m depth) sea surface temperature (SST) can differ from the skin temperature, both the original and updated COARE algorithms include warm layer and cool skin models to extrapolate the bulk SST to the surface [*Fairall et al.*, 1996a]. These models require a first estimate of the full net surface heat flux, including the radiative fluxes. In addition, the diurnal warm layer model requires a first estimate of the wind stress and must be run at timescales that resolve the diurnal cycle (preferably hourly). In cases where hourly data are not available, or where net solar and longwave radiation are not measured or cannot be estimated, then the warm layer and cool skin models cannot be applied. In these cases, default correction values may be used. Incorrect default values, however, can introduce biases in the air-sea temperature difference. Furthermore, because sea surface moisture is computed as the saturated specific humidity (reduced by 2 percent to account for salinity effects) at the surface temperature, biases in the surface temperature can result in biases in the air-sea moisture difference and hence latent heat flux.

[9] As in the original COARE v2.5 algorithm, the v3.0 gustiness parameter, *G*, is based on boundary layer–scale eddies and tuned to hourly averaged values. However, often the flux algorithms are applied to daily (or even monthly) averaged winds. If these averaged winds are a vector

Table 1. Variation in Latent Heat Flux *dQlat* and Sensible Heat Flux *dQsen* Associated With a Unit Variation in the State Variables Sea Surface Temperature T_s, Surface Air Temperature T_a, Surface Air Specific Humidity q_a, Surface Referenced Wind Speed $|\boldsymbol{u} - \boldsymbol{u_s}|$, Relative to Mean Values of $|\boldsymbol{u} - \boldsymbol{u_s}| = 5$ m s^{-1}, $T_s = 26.3$°C, $T_a = 25.4$°C, and $q_a = 17$ g kg^{-1}

	$dQ/d\|\boldsymbol{u} - \boldsymbol{u_s}\|$ *1 m s^{-1}	dQ/dT_s *1°C	dQ/dT_a *1°C	dQ/dq_a *1 g kg^{-1}
dQlat, W m^{-2}	14	29	−3	−20
dQsen, W m^{-2}	1	9	−9	−0

average, then there can be a significant reduction in the vector mean wind speed due to averaging over these subscale shifts in wind direction. Improper representation of this gustiness can lead to substantial errors in the heat fluxes [*Esbensen and McPhaden*, 1996].

[10] To appreciate the sensitivity of the bulk flux calculation to the accuracy of the state variables, that is, to surface referenced winds ($|\boldsymbol{u} - \boldsymbol{u_s}|$), skin temperature ($T_s$), air temperature ($T_a$), and air specific humidity (q_a), in Table 1 we show the deviations in flux associated with the sequential unit deviations from the mean values of the state variables ($|\boldsymbol{u} - \boldsymbol{u_s}| = 5.0$ m s^{-1}, $T_s = 26.3$°C, $T_a = 25.4$°C, $q_a = 17$ g kg^{-1}). Because surface currents can sometimes exceed 1 m s^{-1}, the latent heat flux error introduced by using the Earth referenced winds rather than ocean surface referenced winds can exceed 14 W m^{-2} (Table 1). If the skin temperature differs from the bulk SST by several tenths of a degree, using the uncorrected bulk SST in the algorithm can produce a 5–10 W m^{-2} error in latent heat flux. Indeed, the sensitivity of these fluxes requires not only accurate sensors, but also careful attention to corrections required to make the bulk variables into the expected state variables.

3. Data

3.1. Ship Measurements Near TAO Buoys

[11] TAO buoys have a nominal 1-year deployment and every 6 months a NOAA ship visits each TAO mooring line to recover and deploy moorings and make necessary repairs. As part of enhanced monitoring for the Eastern Pacific Investigation of Climate Processes (EPIC), beginning in November 1999, the NOAA ship tending the 95°W and 110°W TAO mooring lines were equipped by the NOAA Environmental Technology Laboratory (ETL) flux group to monitor boundary layer properties and surface fluxes [*Hare et al.*, 2005; *Fairall et al.*, 1997]. In particular, mean wind speed was measured with a sonic anemometer with full motion corrections [*Edson et al.*, 1998] and corrections for distortion by the ship's structure [*Yelland et al.*, 1998]. Downwelling solar and longwave radiation were measured by Eppley precision pyranometers (PSP) and precision infrared radiometers (PIR). Near-surface (5-cm depth) ocean temperature was measured by a floating temperature sensor (referred to as "sea-snake"). Mean air temperature and relative humidity were measured at 15-m height with aspirated Vaisala HMP-235 sensors. The sonic anemometer/thermometer and a fast-response infrared hygrometer were used to measure the covariance fluxes at 10-min and 1-hour time intervals.

[12] Figure 1 shows a typical 95°W/110°W TAO ship track. During boreal fall cruises (typically in November) the NOAA ship was the *Ronald H. Brown*; during boreal spring cruises (typically March or April) it was the *Ka'imimoana*. No ETL measurements were made on the Spring 2003 TAO 95°W/110°W cruise. However, we include in our intercomparison ETL measurements along the 95°W TAO line in September 2001 aboard the *Ronald H. Brown* as part of the EPIC2001 intensive observational period [*Raymond et al.*, 2004]. All told, there were nine cruises along the TAO lines used for this study between November 1999 and December 2003.

3.2. Suite of Surface Measurements on 95°W and 110°W TAO Buoys During EPIC

[13] The TAO/TRITON array consists of approximately 70 moorings arranged along 11 meridional lines. The 110°W and 95°W lines are the two easternmost and have standard sites at 8°S, 5°S, 2°S, 0, 2°N, 5°N, and 8°N. The standard suite of surface measurements on TAO buoys include wind speed and direction from a R.M. Young wind propeller and vane at 4-m height, air temperature and relative humidity from a Rotronics, Inc. shielded sensor at 3-m height, and bulk sea surface temperature at 1-m depth. The 0, 110°W site has historically been situated next to a subsurface acoustic Doppler current profiler and has carried an Eppley, Inc. solar (PSP) radiometer and a rain gauge.

[14] As part of EPIC-enhanced monitoring from November 1999–December 2003, the easternmost TAO line (95°W) was enhanced with additional moorings and sensors

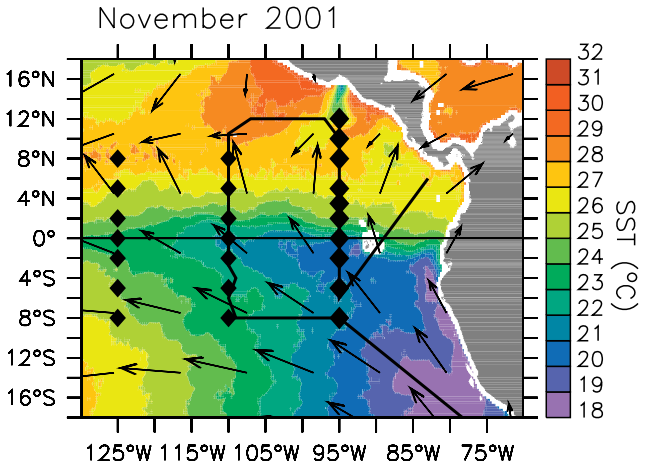

Figure 1. Eastern Pacific Investigation of Climate Processes (EPIC) mooring array shown in relation to November 2001 TRMM Microwave Imager (TMI), sea surface temperature (SST), and QuikSCAT surface winds. Diamonds indicate Tropical Atmosphere Ocean (TAO) buoys. Large diamonds indicate EPIC-enhanced 95°W TAO buoys. The National Oceanic and Atmospheric Administration (NOAA) ship track for November 2001 is indicated by a solid black line.

Table 2. Sensors, Accuracy, Resolution, and Range for Measurements on TAO Next Generation Moorings[a]

Measurement	Sensor Type	Manufacturer: Model	Resolution	Calibration Range	Accuracy
Wind speed	propeller	R.M. Young: 05103	0.2 m s^{-1}	1–20 m s^{-1}	±0.3 m s^{-1} or 3%
Wind direction	vane	R.M. Young: 05103	1.4°	0°–355°	5°–7.8°
Wind direction	fluxgate compass	E.G. and G.: 63764 or KVH: LP101-5	1.4°	0°–359°	
Air temperature	Pt-100 RTD (resistance temperature recorder)	Rotronic Instrument Corp: MP-100	0.01°C	14°–32°C	±0.2°C
Relative humidity	capacitance	Rotronic Instrument Corp: MP-100	.4% RH real time, .02% RH delay mode	55–95% RH	±2.7% RH
Rainfall	capacitance	R.M. Young: 50203-34	0.2 mm h^{-1}	0–50 mm	±0.4 mm h^{-1} on 10-min filtered data
Downwelling shortwave radiation	pyranometer	Eppley Lab.: PSP-TAO, Delrin case	0.4 W m^{-2}	200–1000 W m^{-2}	±1%
Downwelling longwave Radiation	pyrgeometer	Eppley Lab.: PIR-TAO, Delrin case, 3-output	0.1 W m^{-2} 0.03°C	200 W m^{-2} @20°C (thermopile only)	±1%
Sea surface temperature	thermistor	PMEL: NX ATLAS module	0.001°C	6°–32°C	±0.02°C
Ocean current (single point)	Doppler current meter	SonTek: Argonaut-MD	0.1 cm s^{-1} 0.1°	0–200 cm s^{-1}	±5 cm s^{-1}, ±5°

[a]Instrumental accuracies listed are either provided by the manufacturer, or are based on predeployment and postrecovery calibrations and are the root-mean-square drift of the group of sensors, or in the case of the SonTek current profiler, based on intercomparisons between colocated instruments [*Freitag et al.*, 1994, 2001, 2003; *Serra et al.*, 2001; *Lake et al.*, 2003]. Adapted from table published electronically at http://www.pmel.noaa.gov/tao/proj_over/sensors.shtml. TAO, Tropical Atmosphere Ocean.

to form a picket fence of 10 flux sites. The additional 95°W sites at: 3.5°N, 10°N, and 12°N, increase the resolution in the frontal region north of the cold tongue, and extend the line into the warm pool north of the ITCZ (Figure 1). In addition to the standard suite of surface meteorological sensors, the EPIC-enhanced 95°W TAO line carried Eppley, Inc. solar (PSP) and longwave (PIR) radiometers, an R.M. Young rain gauge, a Paroscientific barometric pressure sensor, and a Sontek Argonaut acoustic Doppler current meter (ADCM) to monitor horizontal currents within the 1-m bin centered at 10-m depth. The 5°S–5°N moorings also carried a Sontek ADCM at 40 m, which will not be used in this analysis. Accuracies of these sensors are shown in Table 2. For further information on these sensors, see the works of *Payne et al.* [2002], *Serra et al.* [2001], *Freitag et al.* [2001, 2003], and *Cronin et al.* [2002, 2006].

[15] With the exception of barometric pressure that had an hourly sample rate, all surface measurements had a sample rate of 10 min or faster. Daily averaged values of these variables are telemetered to shore via Service Argos [*McPhaden et al.*, 1998]. High-resolution data are recorded internally and the mooring must be recovered in order to recover the high-resolution data. Thus mooring losses resulted in loss of the high-resolution data for the entire deployment. Unfortunately, being relatively near the coast, and in a highly productive fishery, the 95°W TAO line suffers from human and bird interference. Sensors and buoys are lost more frequently along 95°W than along most other lines, and recovered sensors are sometimes caked with bird guano, or are damaged owing to vandalism. As a result, data return is lower on this line than on most other TAO/TRITON lines, and the data quality indices need to be carefully assessed. Thus air temperature and humidity data in the TAO archives with quality codes of 3–5, indicating lower quality, were not used to compute the latent and sensible heat fluxes and were not used in the statistical ship-buoy intercomparison. When reasonable, data gaps are filled according to procedures discussed below.

3.2.1. Using Daily Averaged Real-Time Data Instead of High-Resolution Data

[16] When moorings are lost, high-resolution time series are not available for the entire deployment. In these cases, we may use the telemetered daily averaged data up until the time at which the mooring failed. For example, for the period November 1999 through December 2003, there was 65% more telemetered wind speeds along 95°W. The telemetered daily averaged wind speed, however, is a vector-averaged wind speed rather than a scalar average, that is, computed from the daily averaged zonal and meridional wind components, rather than from 10-min wind speed time series. In regions with warm water such as at and north of the ITCZ, this gustiness can cause significant variance which is not represented by the daily averaged vector winds and consequently the vector wind speed is biased low relative to the scalar-averaged winds (Figures 2 and 3). We refer to this missing variance as the "mesoscale gustiness," G^2_{meso}. The mean mesocale gustiness can be estimated from hourly winds as

$$\langle G^2_{meso} \rangle = \langle u^2 + v^2 \rangle - \langle \langle u \rangle^2_d + \langle v \rangle^2_d \rangle, \tag{4}$$

where $\langle\ \rangle_d$ indicates a daily average and $\langle\ \rangle$ indicates a record-length average. The COARE bulk algorithm was tuned for hourly averaged state variables and includes a parameterization of the convective gustiness, G, to account for the lost wind variance associated with using an hourly averaged vector wind speed. As shown in Figure 3, the mean mesoscale gustiness is nearly twice as large as the convective gustiness output by the COARE algorithm. Thus, when the telemetered daily averaged data must be used for computing fluxes, we include this mean mesoscale variance (equation (4)) as a function of latitude and the

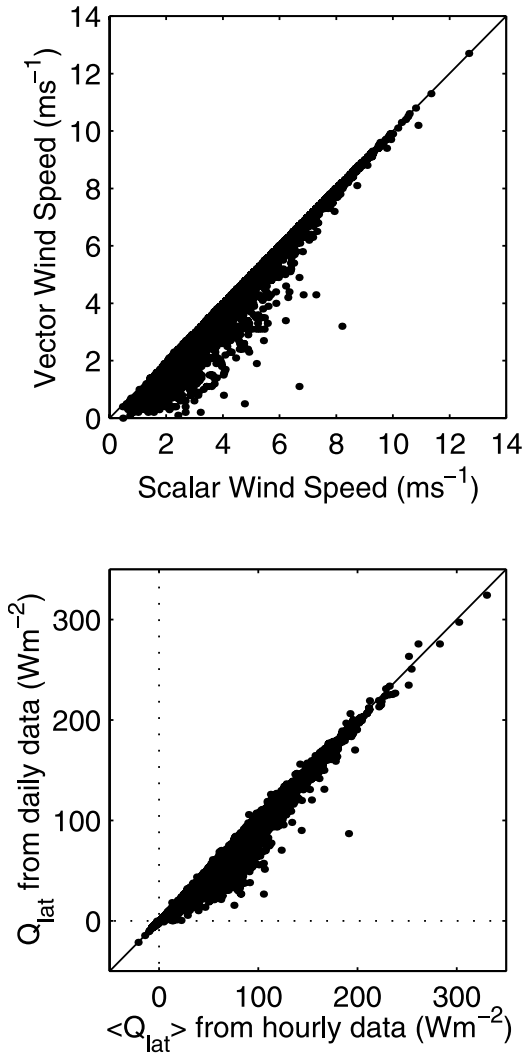

Figure 2. (top) Scatterplot of daily averaged scalar wind speed versus vector wind speed from all 95°W TAO/EPIC buoys. (bottom) The scatterplot of daily latent heat flux computed from hourly data versus from daily averaged data.

variance of the surface referenced winds used in the algorithm is then represented as

$$S^2 = (\langle u \rangle_d - \langle u_s \rangle_d)^2 + (\langle v \rangle_d - \langle v_s \rangle_d)^2 + \langle G^2_{meso} \rangle + G^2, \quad (5)$$

where (u_s, v_s) are the zonal and meridional surface current components. While the mesoscale gustiness may well have subseasonal-interannual variability, we opt for the simple lookup table method that can be generalized for all TAO/TRITON sites. As shown in Figure 3, this simple correction can substantially eliminate the mean bias introduced by the vector daily averaged wind speed. The root-mean square error, however, is still ~5 W m^{-2} in and near the ITCZ region. Further work is needed to evaluate use of a mesoscale gustiness parameterization [e.g., *Zeng et al.*, 2002] for this purpose.

3.2.2. Using OSCAR Currents to Fill Gaps in Ocean Surface Currents

[17] The only TAO/TRITON moorings that routinely monitor upper ocean currents are the equatorial moorings at 165°E, 170°W, 140°W, and 110°W. The shallowest depth (upper bin) measured from nearby ADCP moorings is typically 20- to 30-m depth. During EPIC, 10-m currents were monitored at all ten 95°W; however, these data have many gaps. When possible, gaps in the high-resolution 10-m ocean current data were filled with telemetered daily averaged currents. In cases where no current-meter data were available, the satellite derived 15-m currents from the Ocean Surface Current Analyses–Real time (OSCAR) were used. OSCAR currents are a combination of Ekman and geostrophic currents based on QuikSCAT winds, and TOPEX Poseidon sea level height measurements [*Lagerloef et al.*, 1999; *Bonjean and Lagerloef*, 2002]. A comparison of daily averaged moored 10-m current-meter data and OSCAR currents at 2°N, 95°W is shown in Figure 4. OSCAR currents are only available on 10-day timescale and, for simplicity, we assume that the missing variance associated with the smoothed OSCAR currents is much less than the variance of the winds and therefore can be neglected. Although at this site the latent heat flux computed with the OSCAR surface currents are only marginally better than the heat flux with surface currents set as zero (Figure 4), in regions with large currents the improvement is expected to be more marked.

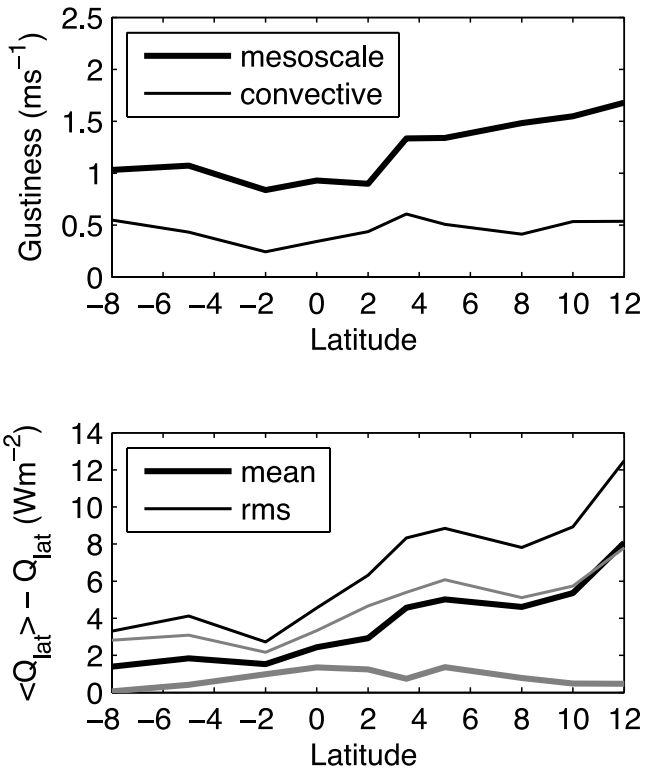

Figure 3. (top) Mean mesoscale gustiness (thick line) and convective gustiness (thin line). (bottom) Mean difference (thick line) and root-mean-square of the difference (thin line) between the daily latent heat flux computed from hourly averages and from daily averaged state variables including daily averaged vector wind speed without any mesoscale gustiness correction (black) and with the mean mesoscale gustiness correction (gray).

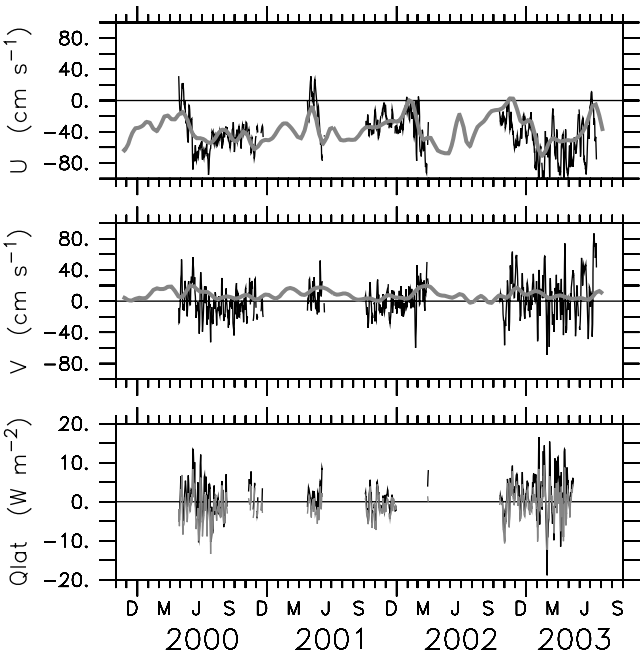

Figure 4. (top) Zonal near-surface velocity at 2°N, 95°W from the daily averaged moored SonTek ADCM at 10 m (dark), and from the Ocean Surface Current Analysis–Real time (OSCAR) product (gray). (middle) Meridional near-surface velocity at 2°N, 95°W from the daily averaged moored SonTek ADCM at 10 m (dark), and from the Ocean Surface Current Analysis–Real time (OSCAR) product (gray). (bottom) Error in the latent heat flux when the surface currents are set to zero (black) or to the OSCAR product (gray).

3.2.3. Using a Parameterization to Fill Gaps in Net Longwave Radiation

[18] As described by *Fung et al.* [1984], there are numerous bulk algorithms for estimating net longwave radiation based on surface conditions. Here we test two parameterizations using daily averaged measurements: those of *Clark et al.* [1974] and *Bunker* [1976]. As shown in Figure 5, both have relatively large scatter with overall RMS differences of 12–15 W m^{-2}. Of the two, the parameterization of *Bunker* [1976] compares somewhat better to observations, with a mean difference of –1 W m^{-2}, and RMS difference of 12 W m^{-2}. It should be noted that the overall standard deviation of the observed net longwave radiation is just 14 W m^{-2} and therefore the *Bunker* [1976] parameterization provides minimal improvement over an estimate set as its mean value.

4. Ship-Buoy Comparison

[19] For brevity, we only show ship and buoy time series along 95°W within the latitudinal bands: 9°S–3.5°S ("southern" sites: 8°S, 5°S) (Figure 6), 3.5°S–1°N ("cold tongue" sites: 2°S, 0) (Figure 7), and 6.5°N–11°N ("ITCZ" sites: 8°N and 10°N) (Figure 8). Typically, the ship transected these bands in 3 days. Thus buoy time series shown in Figures 6–8 were smoothed with a 3-day filter, and ship data were averaged over increments of the diurnal cycle contained within the latitudinal band. In order to get a sense of the data quality, all TAO observations are shown in Figures 6–8, along with their quality codes. However, measurements with lower-quality codes are not used in the latent and sensible heat flux calculation or in the statistical buoy-ship analysis (Table 3).

[20] A striking feature of these time series is the large annual cycle, particularly in the southern and cold tongue sites (Figures 6 and 7). In these bands, specific humidity variations are dominated by the annual cycle. Precipitation has both large seasonal variations and large synoptic (3 day–1 month) variation. In particular, rainfall in the southern band occurs almost exclusively during the warm season from January through May. During this period, winds and net solar radiation are weaker and appear to have increased variability. In contrast, in the ITCZ band, the annual cycle is weaker and subsynoptic variations in rainfall, winds, and net solar radiation are relatively large.

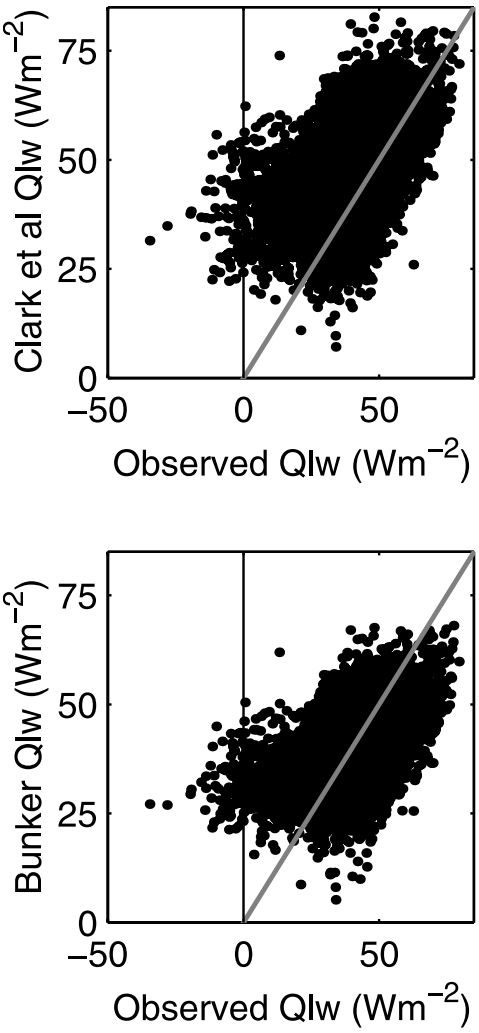

Figure 5. Net longwave radiation parameterization versus observed daily averages from 95°W buoys with longwave radiometers. The *Clark et al.* [1974] parameterization is shown in the top panel, and the *Bunker* [1976] parameterization is shown in the bottom panel. The 1:1 line is shown for comparison.

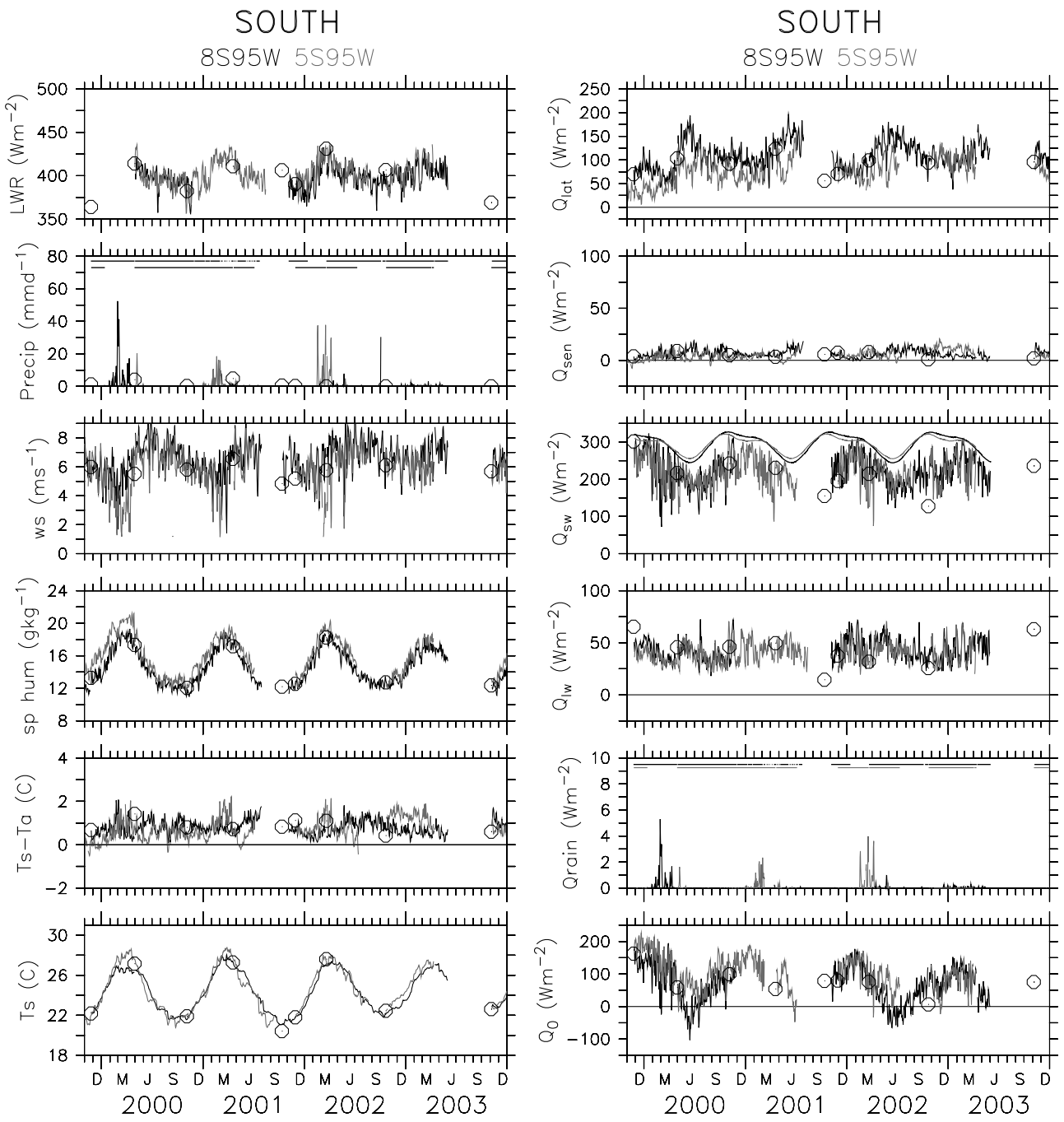

Figure 6. Time series at southern sites within the 9°S–3.5°S band. Left panels show surface measurements: downwelling longwave radiation, precipitation, vector wind speed, specific humidity, sea minus air temperature, and sea surface temperature. Right panels show surface heat flux components: latent heat loss, sensible heat loss, net solar radiation (net solar radiation expected under clear skies is indicated by dashes), net longwave radiation emitted from surface, sensible heat loss due to rainfall, and net surface heat flux into the ocean surface as defined by equation (1). Precipitation data availability is indicated in the panel showing sensible heat flux of rainfall. Latitudinal band averages of the daily average ship measurements are indicated by "o." 8°S, 95°W buoy time series are shown in black; 5°S, 95°W buoy time series are shown in gray.

[21] Overall, the ship and buoy measurements compare quite well in these time series shown in Figures 6–8, although the large subsynoptic variability and the scale of the plots make it difficult to quantitatively assess the comparison. In order to do a statistical comparison, we must decide which buoy the ship should compare to and when. During the EPIC2001 process study, the *Ronald H. Brown* was on station near the 95°W, 10°N buoy for

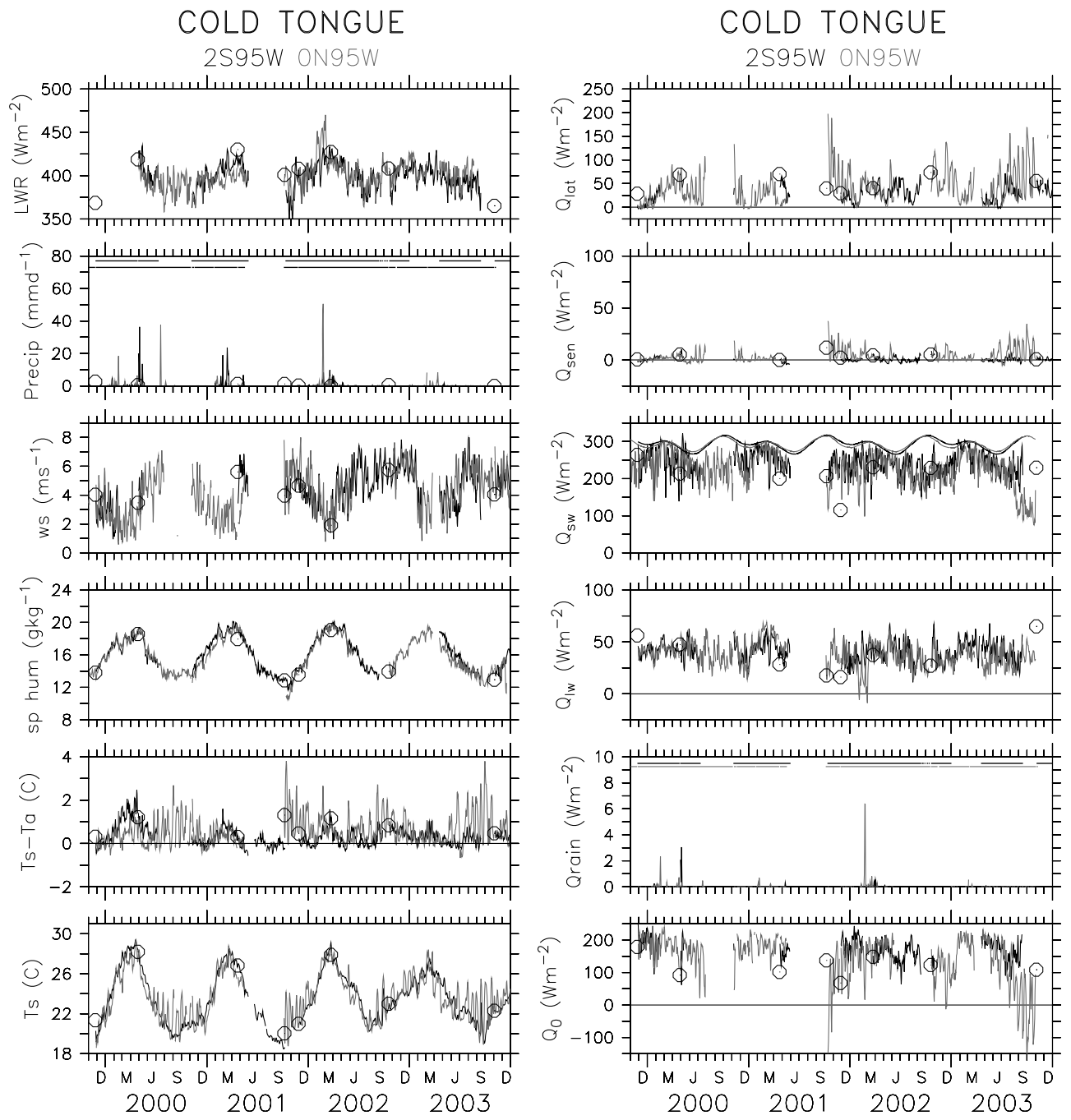

Figure 7. Same as Figure 6 but for time series at cold tongue sites within the 3.5°S–1°N band. 2°S, 95°W buoy time series are shown in black; 0°, 95°W buoy time series are shown in gray.

approximately 17 days in September 2001. The 17-day intercomparisons at this site are shown in Table 3, and only the mean values over these 17 days are included in the full ensemble comparisons in Figures 9 and 10 and Table 3. More typically, the ship was on-station at the mooring site only for the time required for the mooring operations (during which time there are no measurements from an anchored buoy at that site), thus there are few measurements other than the EPIC2001 10°N measurements that satisfy stringent criteria for colocation in time and space required for a quantitative analysis of the ship and buoy differences. We consider ship and buoy measurements to be "colocated" if they were separated by less than ∼10 km at the center of their temporal averaging period. The spatial variability associated with various separations can be represented by a structure function and evaluated with the ship data, as discussed in Appendix A. The comparison was further exasperated by the standard practice of placing the telemetry into fast mode (2-min sampling and telemetry) just prior to deployment, so that the buoy data can be monitored from the ship. "Fast mode" lasts for 12 hours and is not included in the standard processed TAO data. As

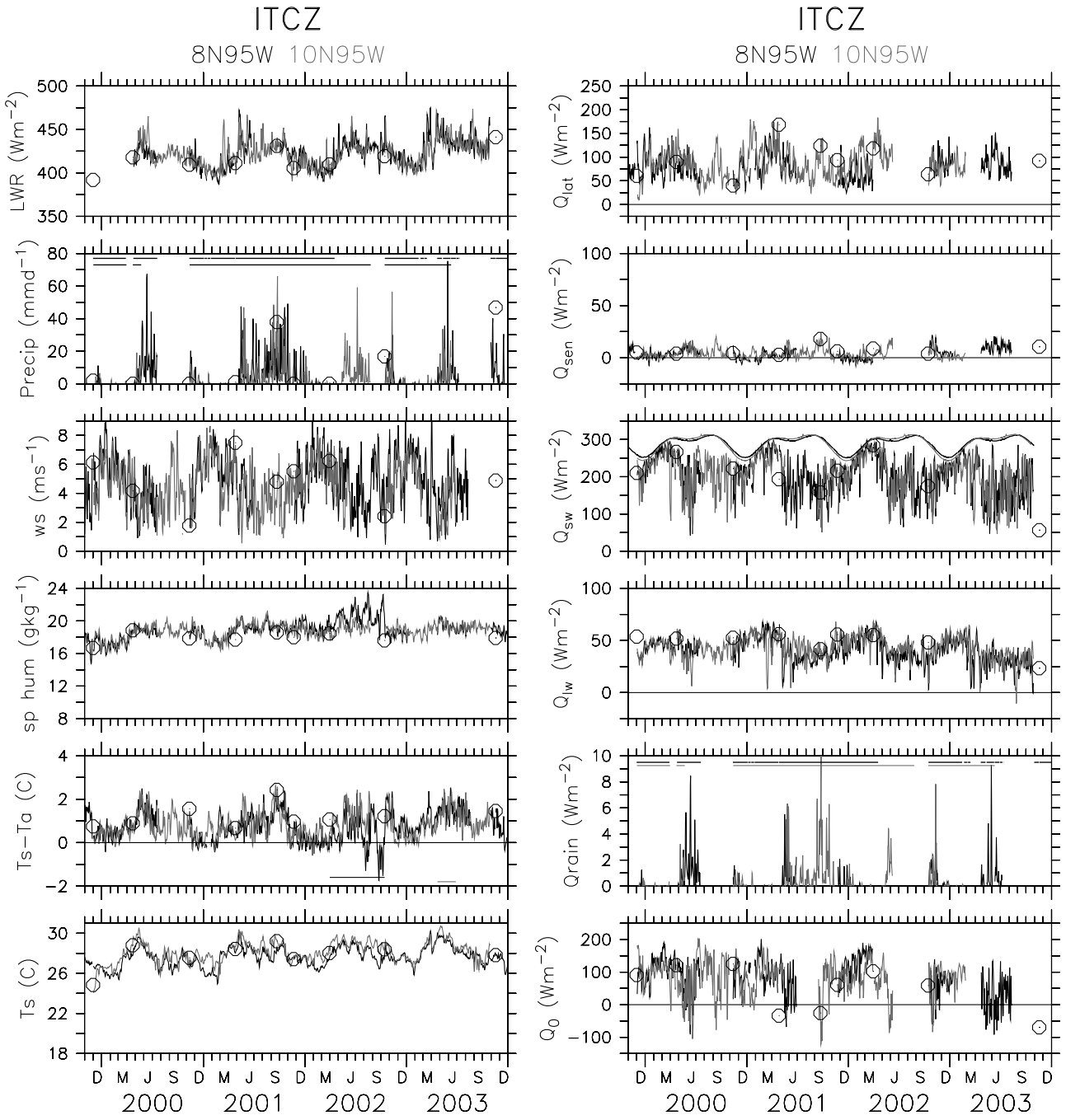

Figure 8. Same as Figure 6 but for time series at intertropical convergence zone (ITCZ) sites within the 6.5°N–11°N band. 8°N, 95°W buoy time series are shown in black; 10°N, 95°W buoy time series are shown in gray. Periods in which the relative humidity and air temperature quality codes indicate lower quality are indicated in the corresponding sea minus air temperature panels; these data are not used in the heat flux calculations.

a consequence, nearly all variables have a 1- to 2-day gap in the daily averaged time series precisely when the ship was nearby. As shown in Table 3 and in the scatterplots for the buoy versus ship meteorological (Figure 9) and heat-flux (Figure 10) measurements, even with the fast-mode data inserted into the high-resolution data (from when the anchor was at rest on the ocean floor), the 9 cruises only produced 11 colocated 6-hour-averaged latent heat flux measurements and 9 colocated daily averaged latent heat flux measurements (with EPIC2001 mean values included as one pair in each set). Specific comments are made below.

4.1. SST

[22] Bulk SST measured from the ship and buoys compare remarkably well, with the buoy SST on average 0–0.1°C cooler than the ship value. Because the ship SST was measured at 5 cm, while the buoy SST was measured at 1-m depth, both are below the cool skin and include a cool skin

Table 3. Buoy Minus Ship Intercomparison of Nearby Daily and 6-Hour-Averaged Values[a]

	Mean (Buoy−Ship) Daily/6 Hour	S.D. (Buoy−Ship) Daily/6 Hour	RMS (Buoy−Ship) Daily/6 Hour	Number of Pairs Daily/6 Hour
$\langle T_s \rangle$, °C	−0.1 (−0.0)/−0.0	0.2 (0.1)/0.1	0.2 (0.1)/0.1	16 (17)/36
$\langle T_a \rangle$, °C	0.3 (0.5)/0.3	0.3 (0.2)/0.2	0.4 (0.5)/0.3	13 (17)/13
$\langle q_a \rangle$, g kg^{-1}	0.6 (0.6)/0.5	0.4 (0.1)/0.4	0.7 (0.7)/0.6	13 (17)/13
$\langle u^2 + v^2 \rangle$, m s^{-1}	0.2 (−0.0)/0.5	0.7 (0.3)/0.6	0.6 (0.3)/0.8	5 (17)/13
$\langle u \rangle^2 + \langle v \rangle^2$, m s^{-1}	0.7 (−0.1)/0.6	0.6 (0.4)/0.8	0.9 (0.4)/1.0	10 (17)/13
$\langle Qsw \rangle$, W m^{-2}	−11 (−11)/−4	NA (17)/26	NA (20)/26	1 (17)/15
$\langle LWR \rangle$, W m^{-2}	−1 (0)/−4	1 (3)/7	1 (3)/6	3 (17)/2
$\langle Qlw \rangle$, W m^{-2}	1 (−2)/3	1 (3)/5	1 (3)/5	3 (17)/2
$\langle Qlat \rangle$, W m^{-2}	−4 (−15)/−12	9 (5)/13	9 (16)/17	9 (17)/11
$\langle Qsen \rangle$, W m^{-2}	−1 (−4)/−3	1 (2)/3	2 (4)/4	9 (17)/11
$\langle Q_0 \rangle$, W m^{-2}	10 (10)/3	NA (15)/44	NA (17)/41	1 (17)/7

[a]Intercomparisons are of values within 10 km. Parentheses show intercomparisons of the daily averaged values when the *Ronald H. Brown* was on station at 10°N 95°W during the EPIC2001 cruise. Six-hourly and daily averaged values from the 10°N 95°W EPIC2001 study are represented as a single mean value in the full ensemble intercomparisons.

bias. The buoy SST measurement is also below the diurnal warm layer and thus is expected to include a warm-layer bias as well. The near-surface thermal stratification, however, can erode and become well mixed through wind mixing and nighttime convection. The mean difference between the ship and buoy SST is thus consistent with very weak (warm layer) thermal stratification in the top meter of the ocean. SST RMS differences are also small (0.1–0.2°C). As shown in the annual cycle of the warm layer correction computed by the bulk algorithm (Figure 11), during the warm season (January–May) near the equator, the average computed warm layer correction is 0.1°C. Elsewhere, the computed warm layer correction tends to be less than 0.05°C. The computed cool skin correction is on average 0.1°C near the equator, and elsewhere is ∼0.2°C (Figure 11). Overall, the cool skin and warm layer corrections tend to cancel each other near the equator during the warm season. Elsewhere in the eastern tropical Pacific, if

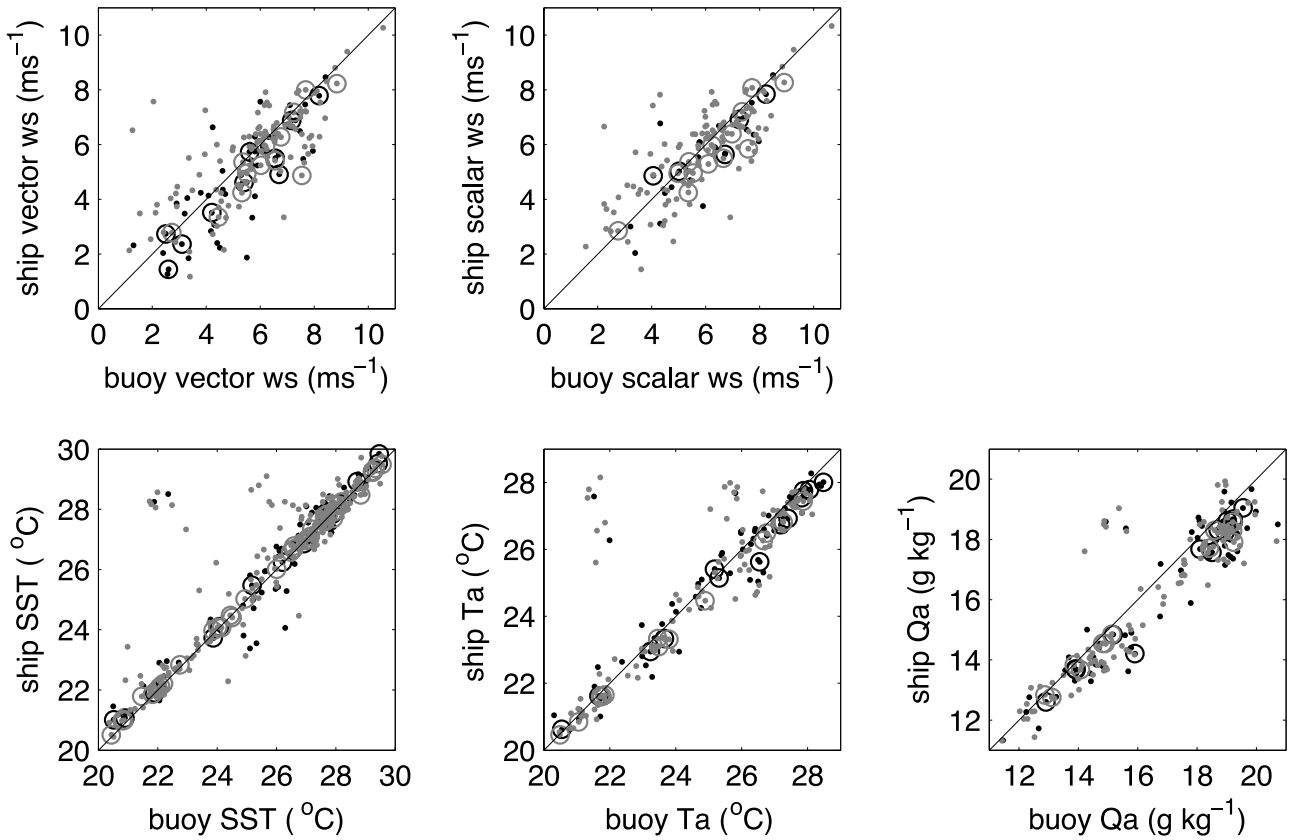

Figure 9. Scatterplots 24-hour-averaged (black) and 6-hour-averaged (gray) state variables from ship and buoys along 95°W and 110°W. Dots indicate measurements from the ship and the nearest buoy. Circles indicate that the ship and buoy were less than ∼10 km apart at the center of the averaging interval.

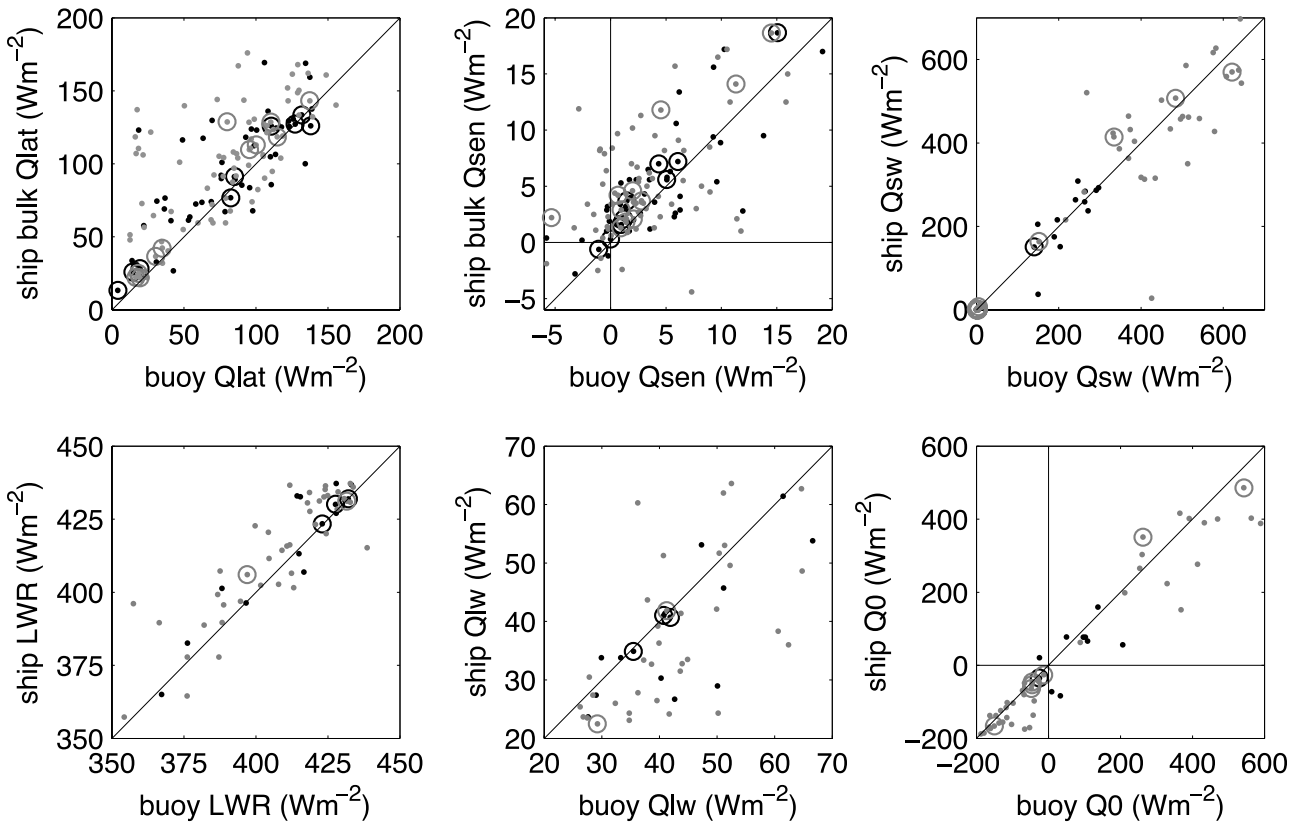

Figure 10. Same as Figure 9 but for surface heat flux measurements. Radiation buoy measurements were limited to 95°W.

solar radiation data are unavailable, it is reasonable to use a default cool skin correction of 0.2°C and no warm-layer correction.

4.2. Air Temperature and Moisture

[23] Prolonged stable stratifications (air temperature warmer than SST), such as seen at 8°N, 95°W (Figure 8), are not realistic. Most of these periods have been flagged as lower quality and are not used in the statistical comparison (Figures 9 and 10 and Table 3) or in the heat flux calculation. Although the ship measurements have been adjusted from 15-m height to the height of the buoy sensor (3 m) based on the stability-corrected logarithmic profile estimated from the flux measurements, the buoy air temperature and specific humidity appear to be on average ~0.3°C and ~0.5 g kg^{-1} higher than that observed by the ship (Table 3). Although the TAO air-temperature sensor has shielding to protect the thermistor from radiative warming, shore-based performance tests show that there can still be warming when winds are low [*Payne et al.*, 2002]. Sensor warming is expected to cause an associated bias in the relative humidity. However, unless there is moisture

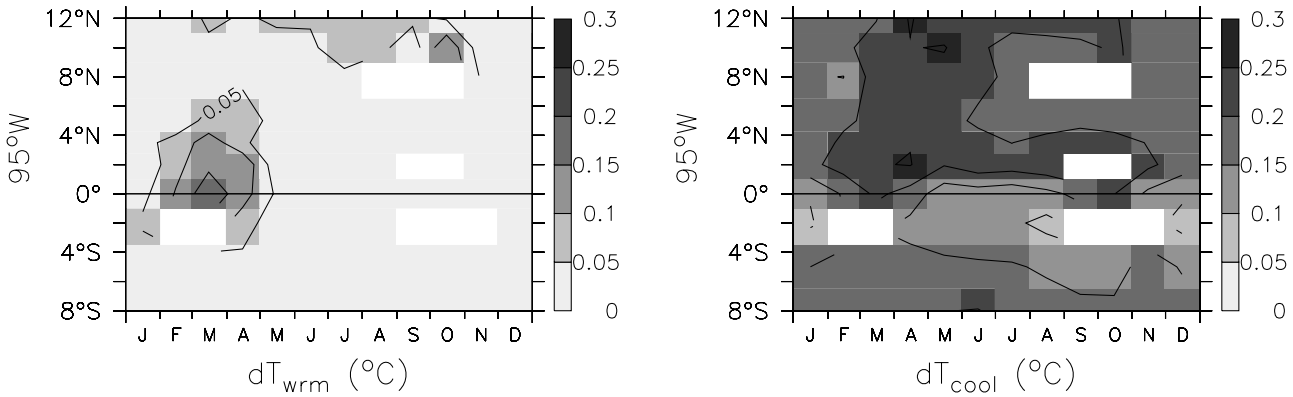

Figure 11. Annual cycle of the warm layer and cool skin temperature corrections along 95°W as estimated from the Coupled Ocean Atmosphere and Response Experiment (COARE) v3.0 bulk algorithm.

exchange occurring within the sensor, the specific humidity should be invariant to sensor warming. In summary, we do not have a good explanation for the observed bias between the ship and buoy specific humidity.

4.3. Wind Speed

[24] As shown in Figures 2 and 3, north of ~3.5°N, 95°W where surface water is warmer than 27°C on average, there can be significant mesoscale gustiness and differences between the scalar and vector wind speeds, particularly when the winds are weak. In these cases, large differences between the ship and buoy wind measurements are likely due to spatial separation, rather than instrumental error. As shown in the time series, however, when averaged over sufficient time and space, the winds appear to be in reasonable agreement. Indeed, the comparison for the scalar wind speed improved when the averaging period increased from 6 hours to 1 day (Table 3).

4.4. Rainfall and the Sensible Heat Flux Due to Rainfall

[25] By the same argument, we do not expect agreement in the 6-hour or daily averaged rain measurements that are separated by ~10 km, and therefore we do not show the scatterplots of the rainfall measurements. However, considering that convective cells typically have scales of a few kilometers and duration less than a few hours, the 3-day-averaged ship and buoy rainfall comparisons within the latitude bands are remarkably good. It is assumed that the temperature of rain is the wet bulb temperature, which can be several degrees cooler than the SST. As shown in Figures 6–8, although the sensible heat flux of rainfall can be relatively large during intense rainfall, on average it is less than 5 W m^{-2}.

4.5. Shortwave and Longwave Radiation

[26] Because we use a constant albedo, we only show the net solar radiation and not the downwelling solar radiation. Solar radiation variability is controlled largely by variations in the zenith angle, and cloud cover. Clear-sky solar radiation time series [*Hare et al.*, 2005; *Cronin et al.*, 2006] are shown in Figures 6–8 here as a reference and to help identify periods with cloud coverage. Clouds absorb and reflect solar radiation and therefore reduce the net solar radiation at the surface. Only 95°W moorings carried both longwave and solar radiometers, and along 110°W, only the equatorial mooring had a solar radiometer. Consequently, there were very few colocated radiation measurements (three daily averaged longwave radiation pairs and only one daily averaged solar radiation pair). As shown in Table 3, the 6-hour-averaged solar radiation pairs had a standard deviation and RMS of 26 W m^{-2}. Assuming a normal distribution, the uncertainty could be reduced to the target level by averaging over ten 6-hour averages, a result consistent with the structure function analysis based on the ship data (see Appendix A). Clouds are expected to enhance the downwelling longwave radiation, although the cloud forcing effect is much weaker than for solar radiation [*Cronin et al.*, 2006]. Discrepancies between the ship and buoy longwave radiation measurements are well within the ±1% manufacturer's specification for accuracy (Table 2). Periods in which the net longwave radiation are parameterized are not included in the ship-buoy comparison of net longwave radiation (Figure 10), but are included in the net surface heat flux and appear to be responsible for some of the large scatter in the 6-hour-averaged values. As discussed earlier, the expected RMS error of the parameterized daily averaged net longwave radiation is 12 W m^{-2} (Figure 5).

4.6. Sensible and Latent Heat Flux

[27] As shown in Table 3, during the EPIC2001 10°N intercomparison, biases in the specific humidity and air temperature resulted in a mean difference in latent heat flux of −15 W m^{-2}. Both the ship and buoy measurements carry their own errors. Assuming the ship and buoy contribute equally but independently to the −15 W m^{-2} difference, their individual errors would be 11 W m^{-2}. Propagation of errors specified in Table 2 produces a latent heat flux error of approximately 10 W m^{-2} [*Cronin and McPhaden*, 1997]. Over the full ensemble, the mean differences in the daily averaged pairs are −4 W m^{-2}. Latent heat flux pairs had an RMS difference of 17 W m^{-2} for 6-hour-averaged pairs, and 9 W m^{-2} for daily averaged pairs. Sensible heat flux pairs had an RMS difference of no more than 4 W m^{-2}. The uncertainty in the buoy estimate of latent heat flux is thus likely to be ~10 W m^{-2}.

4.7. Net Surface Heat Flux

[28] The target uncertainty for net surface heat flux is less than 10 W m^{-2}. As shown in Table 3, while the mean difference between the colocated ship and buoy net surface heat flux pairs are within this target, the scatter among colocated 6-hour-averaged net surface heat flux pairs is much larger than this. The discrepancy, however, is due in large part to the net radiation for which the ship/buoy differences are likely dominated by sampling (and for net longwave radiation, parameterization) error rather than instrumental error. The latitudinal-band time series show qualitative agreement (Figures 6–8). Although the uncertainty in the buoy estimate of net surface heat flux is somewhat larger than the target at 6-hour timescales, we expect that for comparisons at 10 km separation, the target accuracy can be met with averages over 3–4 days. If the buoy flux time series is to be used as a reference for NWP and satellite gridded products, then according to the structure function estimates described in Appendix A, the averaging period must be increased to 2 weeks or more.

5. Comparison to NWP Reanalyses

[29] The cross-validated buoy flux time series are now used as a benchmark data set for comparison with NWP reanalyses fields. Reanalyses combine NWP models and observations (including TAO observations) to produce multidecadal, gridded records of variability suitable for climate studies. However, not all assimilated information is retained in the analysis, owing to the influence of the NWP model physical parameterizations. Previous studies have shown large biases in the surface heat fluxes produced from the reanalyses [*Josey*, 2001; *Wang and McPhaden*, 2001; *Jiang et al.*, 2005; *Cronin et al.*, 2006]. The present study is parallel to the NWP surface cloud forcing assessment by *Cronin et al.* [2006]. As in the work of *Cronin et al.* [2006] and *Wang and McPhaden* [2001], errors are binned into a

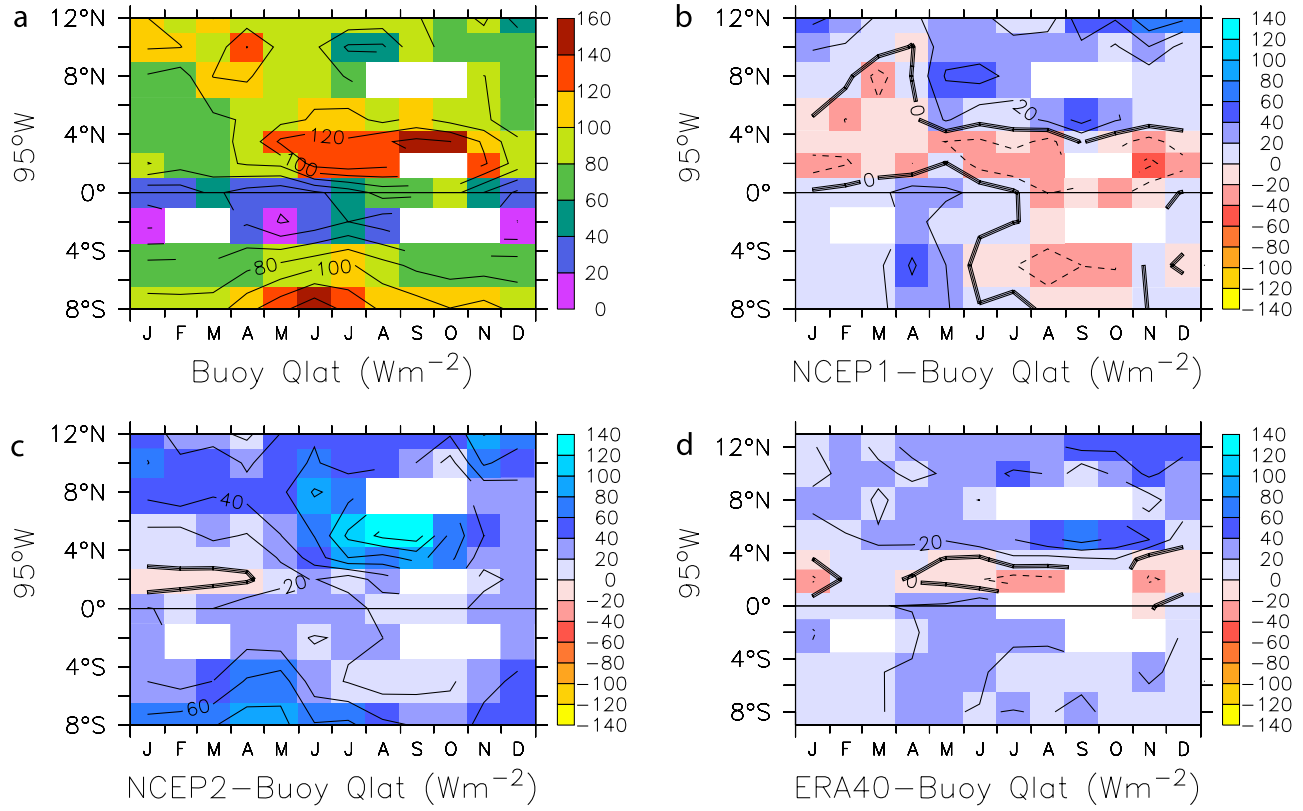

Figure 12. (a) Mean annual cycle of latent heat flux along 95°W from 8°S to 12°N from TAO/EPIC buoy measurements. (b) Mean annual cycle of difference between NWP and buoy latent heat flux field along 95°W from 8°S to 12°N for NCEP1. (c) Mean annual cycle of difference between NWP and buoy latent heat flux field along 95°W from 8°S to 12°N for NCEP2 reanalysis. (d) Mean annual cycle of difference between NWP and buoy latent heat flux field along 95°W from 8°S to 12°N for ERA40. A positive latent heat flux value indicates heat loss by ocean.

seasonal cycle. The *Wang and McPhaden* [2001] analysis of the heat flux products errors, however, was limited to four sites along the equator. Our analysis shows the seasonal cycle of the errors along the 95°W meridian that extends from the stratus deck region at 8°S, across the equatorial cold tongue and north of the ITCZ. The *Jiang et al.* [2005] study covered most of the tropical Pacific; however, it was focused primarily upon the mean biases, rather than the distribution of the errors within the seasonal cycle.

[30] For this comparison, we use the NCEP/NCAR Reanalysis (hereinafter, NCEP1) [*Kalnay et al.*, 1996], the NCEP/DOE Reanalysis (hereinafter, NCEP2) [*Kanamitsu et al.*, 2002] and the ECMWF 40-year Reanalysis (hereinafter ERA40) [*Simmons and Gibson*, 2000]. Both NCEP1 and NCEP2 extend past the study period (November 1999–December 2003). However, ERA40 extends only through July 2002. As a consequence, there are fewer months to compare against the buoy and the analysis is more subject to gaps. Following the methodology used by *Cronin et al.* [2006], monthly averaged NWP values are regridded onto the 10 buoy sites and then differenced from the buoy monthly average. These residuals are then averaged into a seasonal cycle.

[31] NCEP2 uses an updated forecast model, updated data assimilation system, improved diagnostic outputs, and includes fixes to known problems of NCEP1 [*Kanamitsu et al.*, 2002]. It is therefore somewhat surprising that the comparisons against the buoy turbulent and radiative heat fluxes are in fact better for NCEP1 than for NCEP2 (Figures 12–16). However, as shown by *Jiang et al.* [2005], the mean biases for the state variables were in fact better for NCEP2 than for NCEP1. Thus, when *Jiang et al.* [2005] used the COARE algorithm to compute the bulk fluxes from the NWP state variables, the NCEP2 bulk fluxes compared better than the NCEP1 bulk fluxes on average.

[32] All reanalyses appear to have a latent heat loss that is too large in the convective regions. NCEP2, in particular, had errors exceeding 100 W m^{-2} near the ITCZ region during the cool season. Both NCEP1 and ERA40 appear to have somewhat weak latent heat loss in the frontal region, north of the cold tongue, and NCEP1 has too weak latent heat loss throughout the stratocumulus region at and south of the equator during the cool season (Figure 12). In addition, all reanalyses show problems with the radiative heat fluxes (Figures 14 and 15), with too much net solar radiation during the cool season (June–November), when a stratus deck tends to form over the cool southern hemisphere and equatorial cold tongue, and too little net solar radiation in the ITCZ and during the warm season on and south of the equator. These radiative biases are consistent with too little cloud forcing in the reanalyses when the stratus deck tends to form, and too much cloud forcing in

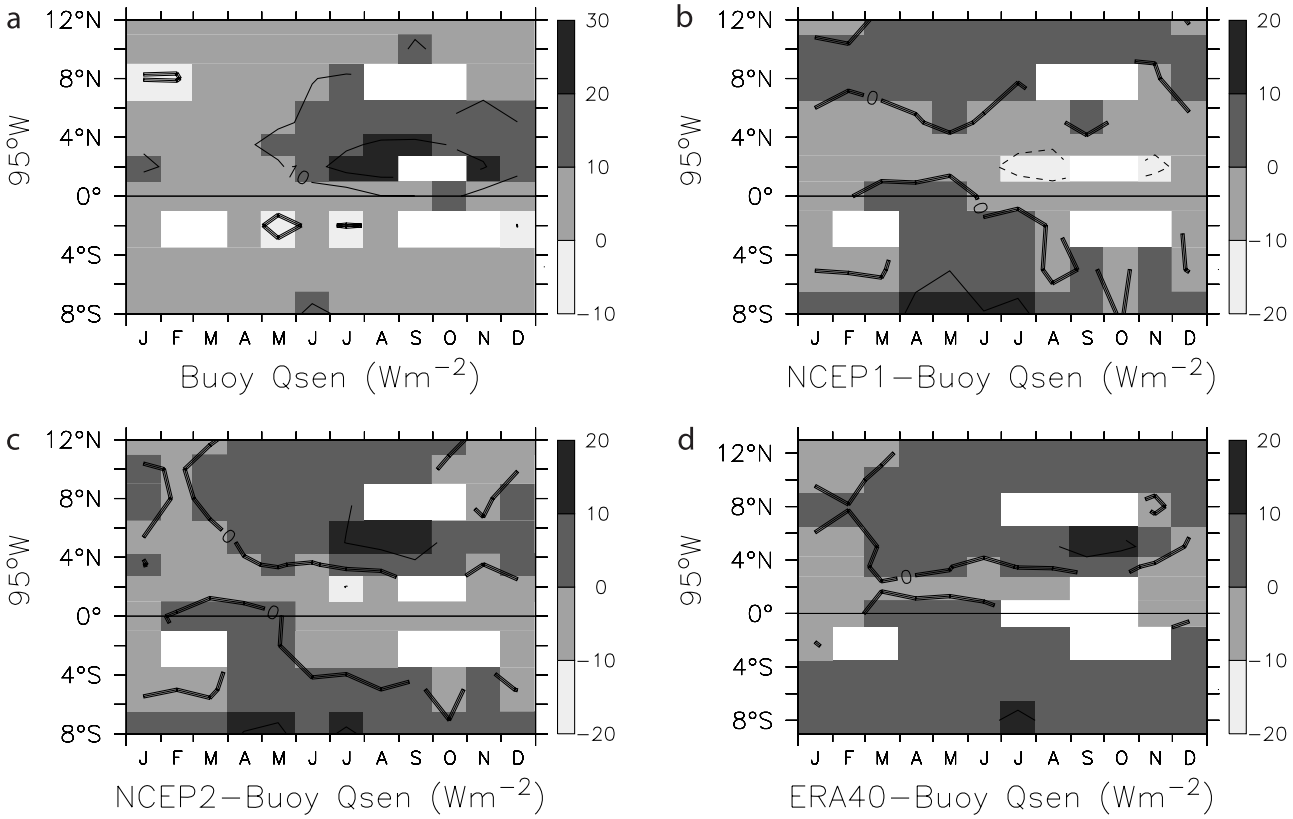

Figure 13. (a–d) Same as Figure 12 but for sensible heat flux.

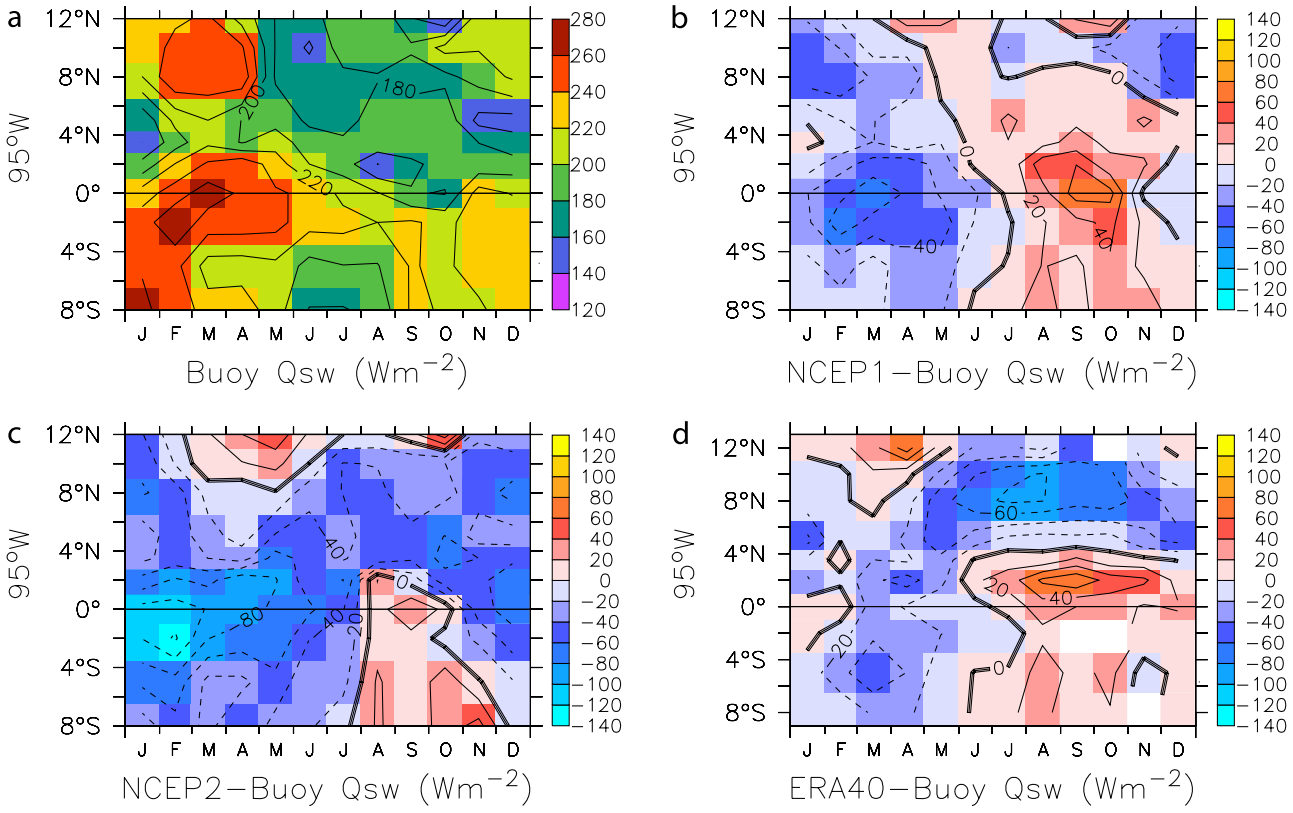

Figure 14. (a–d) Same as Figure 12 but for net solar radiation. A positive net solar radiation value indicates heat gained by ocean.

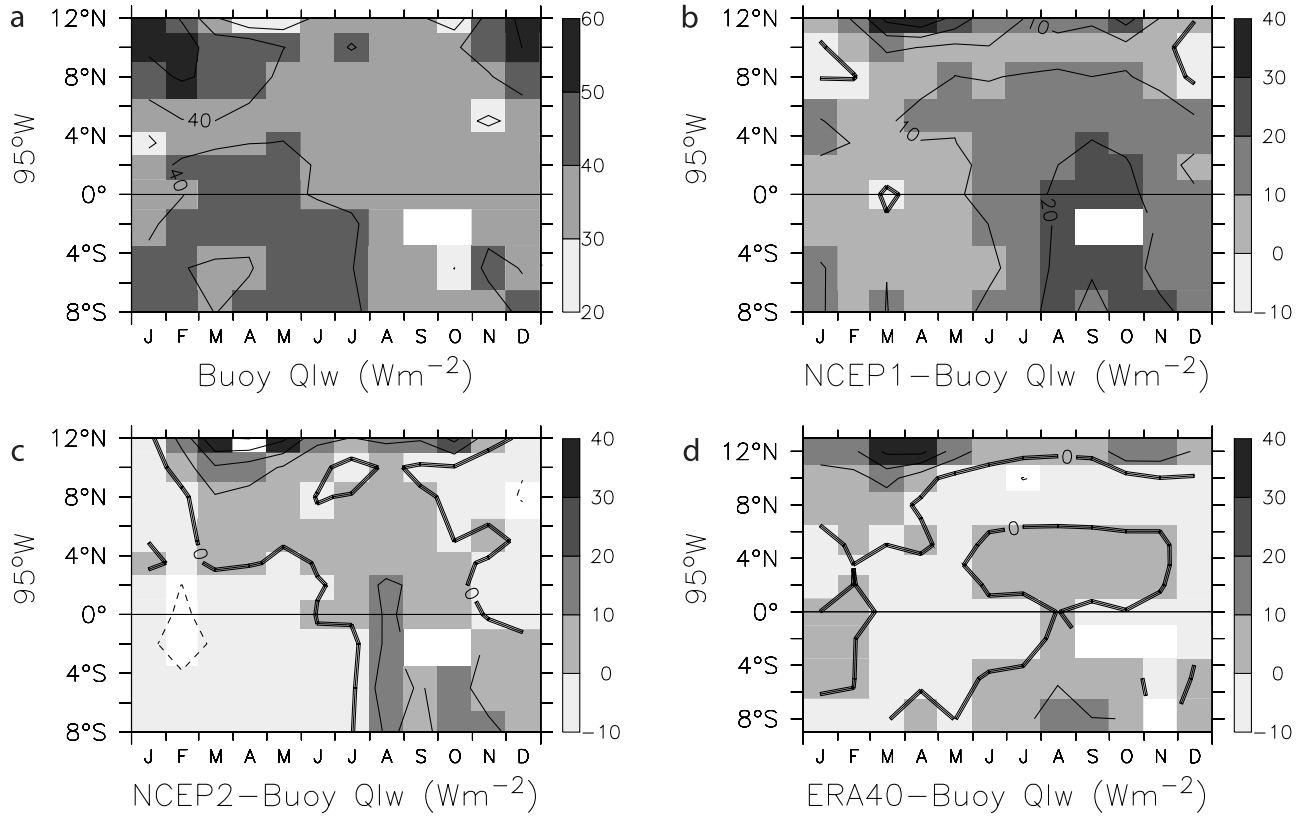

Figure 15. (a–d) Same as Figure 12 but for net longwave radiation. A positive net longwave radiation value indicates heat gain by ocean.

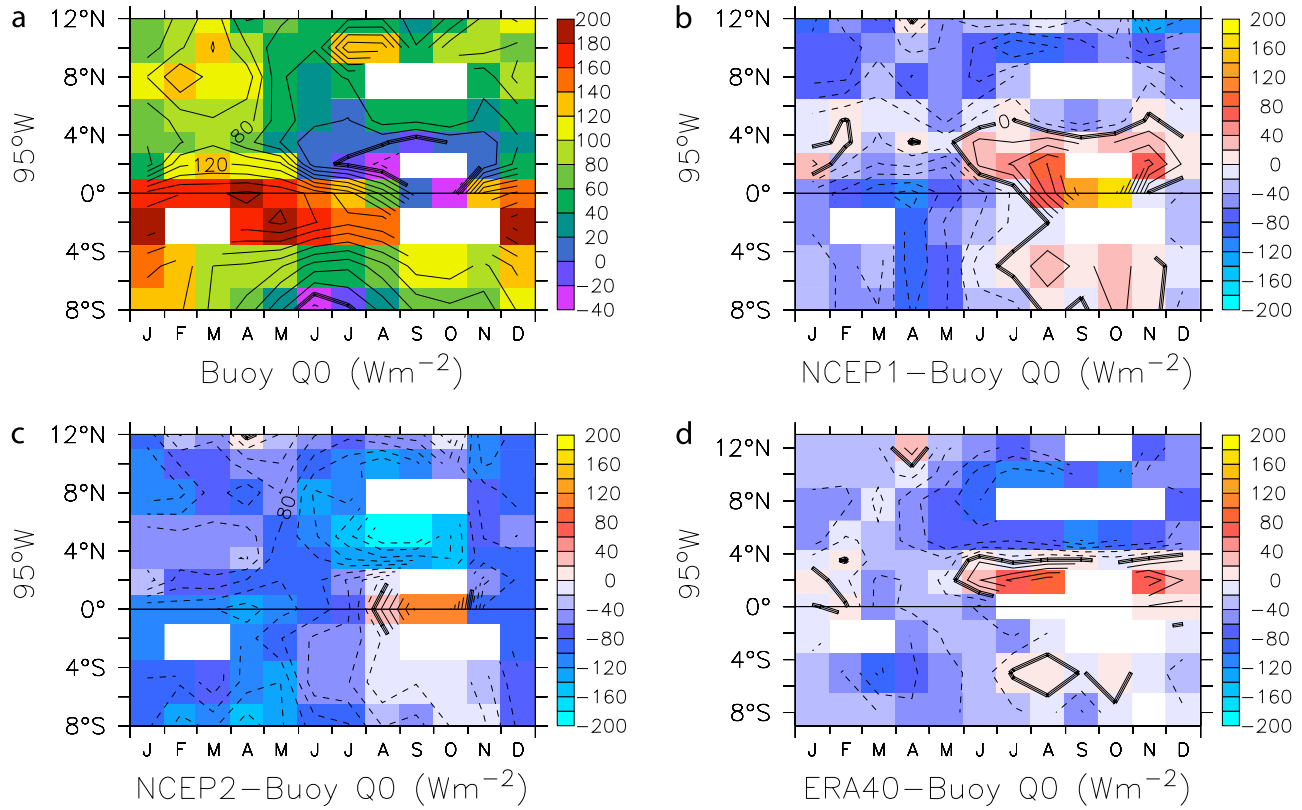

Figure 16. (a–d) Same as Figure 12 but for net surface heat flux (equation (1)). A positive net surface heat flux value indicates heat gained by ocean.

the convective regions, as was found by *Siebesma et al.* [2004] and *Cronin et al.* [2006].

[33] The net result is that NCEP2, and to a lesser extent ERA40, has large negative net surface heat flux (that is, surface heat loss) biases relative to the buoy values. Indeed, whereas the buoy fields show that net surface heat loss tends to be confined to the frontal region during the cold season, and to 8°S during the transition month of June, both NCEP2 and ERA40 have broad regions of net surface heat loss north of the frontal region and for 3 or more months at 8°S. NCEP1 net surface heat flux errors are dominated by the radiative biases, and result in anomalous net surface heat loss in the ITCZ and during the warm season at and south of the equator, and anomalous net surface heat gain at and south of the equator during the cold season when the stratus deck tends to form. These NCEP1 biases, if applied to drive an ocean GCM, would tend to produce a persistent, weak cold tongue and a stratus deck region that, while cooler on average, has anomalous warming during the cool season when stratus is expected to form [*Klein and Hartmann*, 1993].

6. Summary and Conclusion

[34] In the tropics the ocean and atmosphere are tightly coupled, and in the eastern tropical Pacific, variations in the coupled system, such as those associated with ENSO and the annual cycle, can be particularly dramatic. Although climate is by nature the steady or slowly varying patterns, it is highly dependent on variations and noise at subseasonal and even diurnal timescales. In particular, average wind speeds are typically reported as the magnitude of the average wind vector, which can be substantially weaker than the average of the wind speed time series if the wind direction changed orientation over the course of the averaging period. *Esbensen and McPhaden* [1996] found that using daily averaged as opposed to monthly averaged state variables typically produced a 10% enhancement to the latent heat flux, although in the western equatorial Pacific warm pool, this subsynoptic gustiness produced up to a 30% enhancement. In our study we show that using hourly as opposed to daily averaged state variables produced an additional 10% enhancement to latent heat flux. Using daily averaged TAO data rather than the high-resolution data can thus produce an RMS error of up to 12 W m^{-2} in the latent heat flux. Wind speed variance associated with this ''mesoscale'' gustiness is two or three times as large as the convective gustiness parameterized in the COARE algorithm to account for subhourly gustiness. By adding an estimate of the mesoscale gustiness to the daily averaged wind speeds, the turbulent heat flux errors introduced by using daily averaged as opposed to hourly data can be minimized.

[35] The strong diurnal cycle in solar radiation, and thus net surface heat flux, can result in diurnal near surface temperature stratification. COARE measurements showed that on sunny days when the winds were very light, the 1-m depth SST could be 1–2°C cooler than the SST measurements just a few centimeters below the surface [*Soloviev and Lukas*, 1997]. As winds pick up, however, the near surface becomes well mixed. Thus a warm layer correction need be applied only in limited regions and periods or seasons. *Cronin and Kessler* [2002] showed that the SST diurnal cycle on the equator occurred primarily during the warm season. As shown in Figure 11, for the eastern tropical Pacific, the warm layer correction need be considered only during the warm season (January–May) near the equator.

[36] The methodology of calculating air-sea heat fluxes from buoy data should be applicable at any of the nearly 70 TAO/TRITON sites in the Pacific and 10 PIRATA sites in the tropical Atlantic, with the caveat that the analysis has only used data from NextGeneration ATLAS buoys. NextGeneration ATLAS buoys with 10-min internally recorded data were introduced in 1997 in the Atlantic and Pacific. In particular, we recommend using the following:

[37] 1. Hourly averages of the high-resolution 10-min data, whenever possible. When only the telemetered daily averaged data are available, then the missing variance can be estimated from historic data and added to the relative wind speed that is input into the COARE algorithm.

[38] 2. Quality codes provided with the data to ensure that low-quality data are not used in the calculation that requires highly accurate data.

[39] 3. Satellite-generated (OSCAR) surface currents, in lieu of a default value of zero, if direct surface current measurements are unavailable.

[40] 4. *Bunker* [1976] net longwave radiation to infer downwelling longwave radiation, if solar radiation is available, but direct measurement of downwelling longwave radiation is unavailable.

[41] 5. Cool skin and warm layer models to convert the bulk SST into a skin SST estimate. If solar radiation is unavailable, then a default cool skin and warm layer correction can be used. For most of the eastern tropical Pacific, a cool skin correction of ~0.2°C and a warm layer correction of ~0°C are in reasonable agreement with calculated values. In regions with weaker winds, the warm layer correction may be larger, and the cool skin correction may be smaller. On the equator during the warm season (January–May), for example, the warm layer and cool skin corrections tend to cancel.

[42] Comparisons with shipboard data verify the quality of the flux measurements and show that the buoy net surface heat flux measurements appear to have an overall uncertainty near the target 10 W m^{-2}, when careful attention is paid to the state variables. Consequently, enhanced ATLAS buoys may be used as reference sites for satellite and NWP fields when averaged on the order of 2 weeks to a month. Because the 95°W sites are in a region close to land and with strong fisheries, these buoys were subject to interference from humans and birds. It is expected that other lines of buoys in the TAO/TRITON array would perform as well as or better than these shown here.

[43] The cross-validated buoy heat flux data were used as a benchmark to assess the heat flux products from NCEP1, NCEP2, and ERA40. In the convective region, all reanalyses showed too much latent heat loss and too little radiative warming. In the stratocumulus region, NCEP1 showed too little latent heat loss, and all reanalyses showed too much radiative warming. The resulting biases in the NCEP1 net surface heat flux, if applied to drive an ocean GCM, would tend to produce a persistent but weak cold tongue and a cool stratocumulus region with an anomalous annual cycle with

strong warming in August–December when the stratus deck tends to extend northward to the equator. In contrast, an OGCM forced by the NCEP2 net surface heat fluxes would have a large cold bias throughout the entire region. Although the ERA40 net surface heat flux would produce a warm bias in the frontal region, overall, the ERA40 net surface heat flux appears to be the least problematic of the three products.

Appendix A

[44] Because the "colocated" ship and buoy measurements compared in Table 3 were separated by up to 10 km, their differences were due in part to natural spatial variability, as well as to errors in the respective measurements. In this appendix we use the ETL ship-based meteorological time series along 95°W and 110°W to estimate how separation affects the different variables. In particular, we have done a simple analysis of the time series of the ship data from the PACS cruises by computing the mean square difference in measurements as a function of time difference

$$\Delta_x = \overline{[(X(t+\Delta t) - X(t)]^2}. \quad \text{(A1)}$$

This is referred to as the temporal structure function for the atmospheric variable X [*Panofsky and Dutton*, 1984, p. 182]. It represents one aspect of the variability of X caused by turbulent fluctuations in the boundary layer. If we apply Taylor's hypothesis, we can associate the temporal separation with a spatial separation: $\Delta r = U\Delta t$. The structure function is related to the autocorrelation function, R_{xx}, of X by

$$\Delta_x(\Delta r) = 2\left[\sigma_x^2 - R_{xx}(\Delta r)\right], \quad \text{(A2)}$$

where σ_x^2 is the variance of X. The structure function compares measurements from instruments that are not colocated. The structure function can be represented as a function of spatial separation by

$$\Delta_x = C_x^2 \Delta r^m, \quad \text{(A3)}$$

where m is 2/3 for small scales (i.e., in the inertial subrange of isotropic turbulence) and the quantity C_x^2 is called the structure function parameter.

[45] The ETL ship data contain 37000 lines of observations at 10-min time resolution. We have computed Δ for lags of 1 to 100 10-min intervals and done simple fits to equation (A3). The best fit exponent varied from 0.50 (wind speed and downward longwave radiation) to 0.85 (air temperature). Solar radiation required a different treatment because it has a strong temporal variability associated with the diurnal cycle. In this case, we define X as the ratio of the solar flux to the clear-sky flux. We also restricted the analysis to periods when R_{sclr} exceeded 100 W m^{-2}. The results are summarized in Table A1.

[46] The interpretation of Table A1 is as follows. In the case of wind speed, the difference between two identical sensors (i.e., sensors that agree exactly when colocated) separated a distance of 1 km would be characterized by a standard deviation of 0.63 m s^{-1}; if separated by 10 km the standard deviation would increase to 1.1 m s^{-1}. In the case of solar flux, the standard deviation of identical solar radiometers separated 1 km would be 9% of the expected clear-sky solar. If we are comparing two different sensors, each characterized by its own random measurement error σ_a and σ_b, then the variance of the sensor differences as a function of separation is

$$\sigma_{ab}^2 = \overline{[X_a(r+\Delta r) - X_b(\Delta r)]^2} = \sigma_a^2 + \sigma_b^2 + \Delta_x(\Delta r). \quad \text{(A4)}$$

One goal of this paper is the evaluation of the biases of the buoy sensors by comparison with the ship-based system. The mean relative bias of the difference in the two sensors is uncertain by $\sqrt{\sigma_{ab}^2/N}$ where N is the number of coincident observations. In order to make a meaningful comparison, the spatial separation contribution to the uncertainty must be small, that is, roughly less than half the target accuracy. For example, consider the case of air temperature. If we require air temperature measurements to be accurate to within 0.1°C, we need $\sqrt{\Delta_{Ta}(\Delta r)/N} < 0.05$°C. We can meet this requirement by making Δr small and/or N large.

[47] From Table A1 we can evaluate how many observations are required at a given distance so that the spatial separation variability makes a negligible contribution to the uncertainty in the mean bias estimate. For air temperature one 10-min observation is sufficient at a separation of 200 m, 4 at 1 km, 27 at 10 km and 190 at 100 km. For solar flux, we require 5 W m^{-2} accuracy (2%). To eliminate the spatial variability contribution for coincident solar flux measurements requires 75 10-min (or 2 6-hour) observations at a separation of 1 km, 350 (or 10 6-hour) at 10 km and 1681 (or ~12 days) at 100 km. Note this number of observations only refers to the spatial separation aspect of the sample; individual sensor variabilities (σ_a and σ_b) will also contribute to and increase the number of observations needed.

Table A1. Structure Function Exponent m and Structure Function Values at Separations of 1 km, 10 km, and 100 km for 10-Min-Averaged Wind Speed, Air Temperature, Specific Humidity, Downwelling Longwave Radiation, Downwelling Solar Radiation Scaled by the Clear-Sky Value, Latent Heat Flux, and Sensible Heat Flux[a]

Variable	m	$\sqrt{\Delta_x(1\,km)}$	$\sqrt{\Delta_x(10\,km)}$	$\sqrt{\Delta_x(100\,km)}$
U, m s^{-1}	0.50	0.63	1.1	2.0
T_a, °C	0.85	0.10	0.26	0.69
q_a, g kg^{-1}	0.67	0.13	0.28	0.69
R_l, W m^{-2}	0.50	6	11	19
R_s/R_{sclr}	0.67	0.09	0.19	0.41
$Qlat$, W m^{-2}	0.67	8.9	19	40.6
$Qsen$, W m^{-2}	0.67	1.7	3.6	7.8

[a]For the clear-sky value, see text.

[48] **Acknowledgments.** The authors thank NCEP, ECMWF, and the OSCAR project office for providing data used in this analysis. NCEP reanalyses data were accessed through http://nomad2.ncep.noaa.gov:9090/dods/reanalyses/ through the Distributed Oceanographic Data System (DODS). ECMWF ERA40 data were downloaded from the ECMWF data server http://www.ecmwf.int/. OSCAR data were obtained from http://www.oscar.noaa.gov/. The authors also wish to thank C. Fey and J. Hare for their help in processing the data. This research was supported by grants from NOAA Office of Global Programs, Pan American Climate Studies,

and the Ocean Climate Offices. This publication is PMEL contribution 2869.

References

Bonjean, F., and G. S. E. Lagerloef (2002), Diagnostic model and analysis of the surface currents in the tropical Pacific Ocean, *J. Phys. Oceanogr.*, *32*, 2938–2954.

Bunker, A. F. (1976), Computation of surface energy flux and annual air-sea cycle of the North Atlantic Ocean, *Mon. Weather Rev.*, *104*, 1122–1140.

Clark, N. E., L. Eber, R. M. Laurs, J. A. Renner, and F. F. T. Saur (1974), Heat exchange between ocean and atmosphere in the eastern North Pacific for 1961–71, *NOAA Tech. Rep. NMFS SSRF, 682*.

Cronin, M. F., and W. S. Kessler (2002), Seasonal and interannual modulation of mixed layer variability at 0, 110°W, *Deep Sea Res., Part I*, *49*, 1–17.

Cronin, M. F., and M. J. McPhaden (1997), The upper ocean heat balance in the western equatorial Pacific warm pool during September–December 1992, *J. Geophys. Res.*, *102*, 8533–8553.

Cronin, M. F., N. Bond, C. Fairall, J. Hare, M. J. McPhaden, and R. A. Weller (2002), Enhanced oceanic and atmospheric monitoring underway in eastern Pacific, *Eos Trans. AGU*, *83*(19), 205.

Cronin, M. F., N. A. Bond, C. Fairall, and R. A. Weller (2006), Surface cloud forcing in the east Pacific stratus deck/cold tongue/ITCZ complex, *J. Clim.*, *19*, 392–409.

DeSzoeke, S. P., C. S. Bretherton, N. A. Bond, M. F. Cronin, and B. Morley (2005), EPIC 95°W observations of the eastern Pacific atmospheric boundary layer from the cold tongue to the ITCZ, *J. Atmos. Sci.*, *62*, 426–442.

Edson, J. B., A. A. Hinton, K. E. Prada, J. E. Hare, and C. W. Fairall (1998), Direct covariance flux estimates from mobile platforms at sea, *J. Atmos. Oceanic Technol.*, *15*, 547–562.

Esbensen, S. K., and M. J. McPhaden (1996), Enhancement of tropical ocean evaporation and sensible heat flux by atmospheric mesoscale systems, *J. Clim.*, *9*, 2307–2325.

Fairall, C. W., E. F. Bradley, J. S. Godfrey, G. A. Wick, J. B. Edson, and G. S. Young (1996a), Cool-skin and warm-layer effects on sea surface temperature, *J. Geophys. Res.*, *101*, 1295–1308.

Fairall, C. W., E. F. Bradley, D. P. Rogers, J. B. Edson, and G. S. Young (1996b), Bulk parameterization of air-sea fluxes for Tropical Ocean–Global Atmosphere Coupled-Ocean Atmosphere Response Experiment, *J. Geophys. Res.*, *101*, 3747–3764.

Fairall, C., A. B. White, J. B. Edson, and J. Hare (1997), Integrated shipboard measurements of the marine boundary layer, *J. Atmos. Oceanic Technol.*, *14*, 338–359.

Fairall, C. F., E. F. Bradley, J. E. Hare, A. A. Grachev, and J. B. Edson (2003), Bulk parameterization of air-sea fluxes: Updates and verification for the COARE algorithm, *J. Clim.*, *16*, 571–591.

Frietag, H. P., Y. Feng, L. J. Mangum, M. P. McPhaden, J. Neander, and L. D. Stratton (1994), Calibration procedures and instrumental accuracy estimates of TAO temperature, relative humidity and radiation measurements, *NOAA Tech. Mem. ERL PMEL-104*, Natl. Oceanic and Atmos. Admin./Pac. Mar. Environ. Lab., Seattle, Wash.

Freitag, H. P., M. O'Haleck, G. C. Thomas, and M. J. McPhaden (2001), Calibration procedures and instrumental accuracies for ATLAS wind measurements, *NOAA Tech. Mem. OAR PMEL-119*, Natl. Oceanic and Atmos. Admin./Pac. Mar. Environ. Lab., Seattle, Wash.

Freitag, H. P., M. J. McPhaden, C. Meinig, and P. Plimpton (2003), Mooring motion bias of point Doppler current meter measurements, paper presented at Seventh Working Conference on Current Measurement Technology, Inst. of Electr. and Electron. Eng., San Diego, Calif., 13 – 15 March .

Fung, I. Y., D. E. Harrison, and A. A. Lacis (1984), On the variability of the net longwave radiation at the ocean surface, *Rev. Geophys.*, *22*, 177–193.

Gentemann, C. L., F. J. Wentz, C. A. Mears, and D. K. Smith (2004), In situ validation of Tropical Rainfall Measuring Mission microwave sea surface temperatures, *J. Geophys. Res.*, *109*, C04021, doi:10.1029/2003JC002092.

Hare, J. E., C. W. Fairall, T. Uttal, D. Hazen, M. F. Cronin, N. A. Bond, and D. E. Veron (2005), Cloud, radiation, and surface forcing in the equatorial eastern Pacific, *NOAA Tech. Mem. OAR-PSD 307*, 64 pp., Natl. Oceanic and Atmos. Admin./Earth Syst. Res. Lab., Boulder, Colo.

Jiang, C.-L., M. F. Cronin, K. A. Kelly, and L. Thompson (2005), Evaluation of a hybrid satellite- and NWP-based turbulent heat flux product using Tropical Atmosphere-Ocean (TAO) buoys, *J. Geophys. Res.*, *110*, C09007, doi:10.1029/2004JC002824.

Josey, S. A. (2001), A comparison of ECMWF, NCEP-NCAR, and SOC surface heat fluxes with moored buoy measurements in the subduction region of the northeast Atlantic, *J. Clim.*, *14*, 1780–1789.

Kalnay, E., et al. (1996), The NCEP/NCAR 40–year Reanalysis Project, *Bull. Am. Meteorol. Soc.*, *77*, 437–471.

Kanamitsu, M., W. Ebisuzaki, J. Woollen, S.-K. Yang, J. J. Hnilo, M. Fiorino, and G. L. Potter (2002), NCEP-DEO AMIP-II Reanalysis (R-2), *Bull. Am. Meteorol. Soc.*, *83*, 1631–1643.

Klein, S. A., and D. L. Hartmann (1993), The seasonal cycle of low stratiform clouds, *J. Clim.*, *6*, 1587–1606.

Lagerloef, G. S. E., G. Mitchum, R. Lukas, and P. Niiler (1999), Tropical Pacific near-surface currents estimated from altimeter, wind and drifter data, *J. Geophys. Res.*, *104*, 23,313–23,326.

Lake, B. J., S. M. Noor, H. P. Freitag, and M. J. McPhaden (2003), Calibration procedures and instrumental accuracy estimates of ATLAS air temperature and relative humidity measurements, *NOAA Tech. Mem. OAR PMEL-123*, Natl. Oceanic and Atmos. Admin./Pac. Mar. Environ. Lab., Seattle, Wash.

Liu, W. T., K. B. Katsaros, and J. A. Businger (1979), Bulk parameterization of air-sea exchanges of heat and water vapor including the molecular constraints at the interface, *J. Atmos. Sci.*, *36*, 1722–1735.

McPhaden, M. J., et al. (1998), The tropical ocean global atmosphere (TOGA) observing system: A decade of progress, *J. Geophys. Res.*, *103*, 14,169–14,240.

Panofsky, H. A., and J. A. Dutton (1984), *Atmospheric Turbulence: Models and Methods for Engineering Applications*, 397 pp., John Wiley, Hoboken, N. J.

Payne, R. E., et al. (2002), A comparison of buoy meteorological systems, *WHOI Tech. Rep. WHOI-2002–10*, Woods Hole Oceanogr. Inst., Woods Hole, Mass.

Raymond, D. J., S. K. Esbensen, M. Gregg, C. S. Bretherton, L. K. Shay, T. Uttal, and P. Zuidema (2004), EPIC2001 and the coupled ocean-atmosphere system of the tropical East Pacific, *Bull. Am. Meteorol. Soc.*, *85*, 1341–1354.

Serra, Y. L., P. A'Hearn, H. P. Freitag, and M. J. McPhaden (2001), ATLAS self-siphoning rain gauge error estimates, *J. Atmos. Oceanic Technol.*, *18*, 1989–2002.

Servain, J., A. J. Busalacchi, M. J. McPhaden, A. D. Moura, G. Reverdin, M. Vianna, and S. E. Zebiak (1998), A Pilot Research Moored Array in the Tropical Atlantic (PIRATA), *Bull. Am. Meteorol. Soc.*, *79*, 2019–2031.

Siebesma, A. P., et al. (2004), Cloud representation in general-circulation models over the northern Pacific Ocean: A EUROCS intercomparison study, *Q. J. R. Meteorol. Soc.*, *130*, 3245–3267.

Simmons, A. J., and J. K. Gibson (Eds.) (2000), *The ERA-40 Project Plan*, *ERA-40 Proj. Rep. Ser. 1*, 62 pp., Eur. Cent. for Medium-Range Weather Forecasts, Reading, U. K.

Soloviev, A., and R. Lukas (1997), Observation of large diurnal warming events in the near-surface layer of the western equatorial Pacific warm pool, *Deep Sea Res., Part I*, *44*, 1055–1076.

Sui, C.-H., X. Li, M. M. Rienecker, K.-M. Lau, I. Laszlo, and R. T. Pinker (2003), The role of daily surface forcing in the upper ocean over the tropical Pacific: A numerical study, *J. Clim.*, *15*, 756–766.

Vialard, J., A. T. Weaver, D. L. T. Anderson, and P. Delecluse (2003), Three- and four- dimensional variational assimilation with a general circulation model of the tropical Pacific Ocean, part II, Physical validation, *Mon. Weather Rev.*, *131*, 1379–1395.

Wang, W., and M. J. McPhaden (2001), What is the mean seasonal cycle of surface heat flux in the equatorial Pacific?, *J. Geophys. Res.*, *106*, 837–857.

Yelland, M. J., B. I. Moat, P. K. Taylor, R. W. Pascal, J. Hutchings, and V. C. Cornell (1998), Wind stress measurements from the open ocean corrected for airflow distortion by the ship, *J. Phys. Oceanogr.*, *28*, 1511–1526.

Zeng, X., Q. Zhang, D. Johnson, and W.-K. Tao (2002), Parameterization of wind gustiness for the computation of ocean surface fluxes at different spatial scales, *Mon. Weather Rev.*, *130*, 2125–2133.

M. F. Cronin and M. J. McPhaden, Pacific Marine Environmental Laboratory, NOAA, 7600 Sand Point Way NE, Seattle, WA 98115, USA. (meghan.f.cronin@noaa.gov)

C. W. Fairall, Earth System Research Laboratory, NOAA, Boulder, CO 80305, USA.